RICE UNIVERSITY

Magnetic helicity injection and velocity characteristics of rotating sunspots

by

Chunming Zhu

A Thesis Submitted
in Partial Fulfillment of the
Requirements for the Degree

Master of Science

Approved, Thesis Committee:

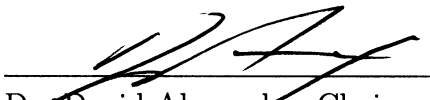

Dr. David Alexander, Chair
Professor of Physics and Astronomy

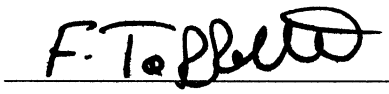

Dr. Frank Toffletto
Professor of Physics and Astronomy

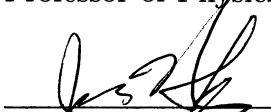

Dr. Jason H. Hafner
Associate Professor of Physics and
Astronomy and Chemistry

Houston, Texas

November, 2010

ABSTRACT

Magnetic helicity injection and velocity characteristics of rotating sunspots

by

Chunming Zhu

This thesis presents calculations of the magnetic helicity injection due to rotating sunspots and a determination of the characteristics of the rotating sunspots in the active regions with simple magnetic configurations.

Four active regions are investigated to study the relationship between rotating sunspots and magnetic helicity. The observations indicate that significantly more helicity is injected during the period of rotation in polarities with strong magnetic field. This may be a result of the emergence of a magnetic flux rope from below the solar surface. Moreover, our preliminary study on a large sample of 90 active regions shows that the level of flaring activity increases with the rate of helicity injection.

Finally, a statistical study is carried out to determine the relation between rotating sunspots and the emergence of magnetic flux tubes. Among 82 active regions which exhibit flux emergence, 93% are associated with rotating sunspots. Among 50 active regions without well-defined flux emergence, 60% of sunspots are observed to be rotating, though relatively slowly. In addition, we find that sense of the rotation (i.e., clockwise or counter-clockwise) of the sunspots shows a weak hemispherical tendency.

Acknowledgments

First of all, I would express great thanks to my superadvisor, Dr. David Alexander, for his advice and patience. I feel honored to be a graduate student of Dr. Alexander. His guidance and support have helped me in all the time of research and writing of this thesis.

I am very grateful to Dr. Lirong Tian, whose suggestions and insights have been incorporated into this thesis. Also, I thank Dr. Yuhong Fan, whose knowledge and discussions have enlighten me on the present and future study.

Great thanks to Dr. Frank Toffletto, and Dr. Jason Hafner, for their dedication as the committee members for this thesis.

I also thank the faculties and fellow students in our department of physics and astronomy. Their stimulating suggestions, insights and discussions, have help me with the improvement of this thesis.

I would thank my family members, especially my wife, Haixia Liu, for supporting and encouraging me through these years.

Contents

Illustrations

Tables

Chapter 1

Introduction

This chapter presents a brief introduction to sunspot observations and magnetic helicity, the main topics of this thesis. In section 1, the general features of sunspots are introduced. This is followed by an introduction to magnetic helicity, including its definition and calculation in section 2. Finally, some descriptions of the instruments of SOHO (the Solar and Heliospheric Observatory) and TRACE (Transition Region and Coronal Explorer) that are used in our analysis are included in section 3.

1.1 Sunspot observations

Sunspots are magnetic structures that appear on the solar photosphere. They are visibly dark spots compared to the surrounding areas. Their average magnetic filed strength is about 1000 – 1500 G, but can go as high as 3000 – 4000 G. As a result of its intense magnetic field, which inhibits convection of heat to the solar surface, a sunspot is about 1600 K cooler than the quiet sun. Because the brightness is proportional to the fourth power of the temperature, the sunspots are about 25% as bright as the rest of the photosphere, and show up as dark regions (see Alexander, 2009).

Sunspots can have a range of sizes (Solanki, 2003), with the diameters of very large sunspots as high as 60 Mm. However, the smallest sunpots are only about 3.5 Mm in diameter.

1.1.1 Magnetic structures of sunspots

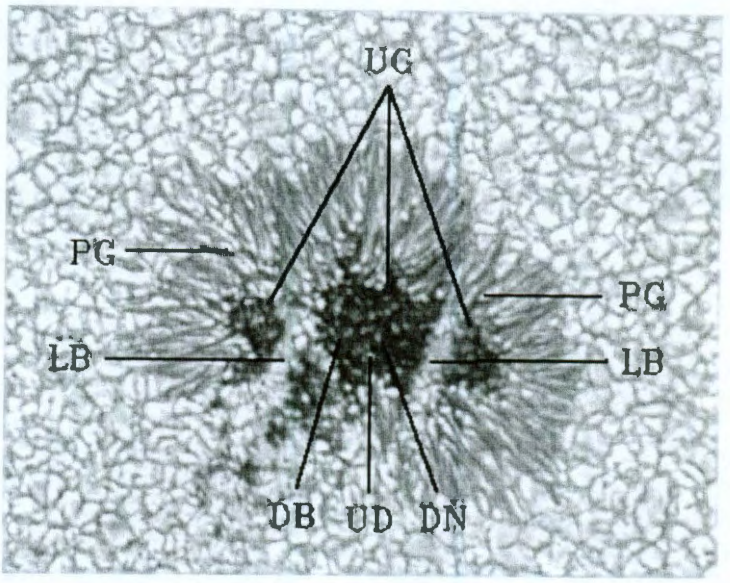

Figure 1.1 : Fine structures of a sunspot (From Sobotka, 1997). DB: diffuse background, DN: dark nucleus, LB: light bridge, PG: penumbral grain, UC: umbral core, UD: umbral dot.

Each sunspot is composed mainly of two structures: the *umbra* which is the dark core, and the *penumbra* which is the less dark halo. When a sunspot is observed at a high spatial resolution (e.g. greater than 1″), some fine structures can be identified. These small-scale features include: umbral cores, penumbral grains, light bridges, dark nucleus, umbral dots and a diffuse background. These structures are shown in figure 1.1.

1.1.2 Evolution

Associated with sunspots are regions of high activity powered by the magnetic field of the sunspot. These are known as *active regions* and are evident in enhanced

emission at all levels in the solar atmosphere. The evolution of sunspots in an active region is described in the review paper of Solanki (2003). At the beginning, individual pores begin to form at the photosphere with the emergence of magnetic flux. Later these pores move towards those with the same polarity and coalesce into larger ones. When the diameter of a pore exceeds about 3.5 Mm, it begins showing penumbral structure and becomes a sunspot. Then, after they are completely formed, the sunspots start to decay. Observations show that sunspots can stay on the photosphere for hours to months. Sunspots of bigger size stay longer than the smaller ones.

The orientation of the magnetic polarities of the sunspots changes with each solar cycle ($\sim$ 11 years). This is known as the Hale polarity law (Hale et al., 1919). Generally, the polarities of *leading* and *following sunspots* (leading and following are defined with respect to the direction of solar rotation) in each active region remains the same in each hemisphere for a 11-year solar cycle, with the leading polarities opposite to those on the other hemisphere. The orientation of the magnetic fields reverses at the solar minima between two successive solar cycles.

In addition, sunspots in each solar cycle show latitude migration, which is known as Spörer's law. At the beginning of a solar cycle, the sunspots appear at a latitude of about 30°–35° in both hemispheres. Then, as the solar cycle progresses, the locations of sunspots' appearance migrate to lower latitude, until they appear within $\pm 10°$ of the solar equator at the end of the solar cycle (Stix, 2002). The latitude migration is frequently shown in what is called the butterfly diagram* (Maunder, 1922), as shown in Fig. 1.2.

Another important and interesting phenomenon is called Joy's law, which describes the tilt angle between two polarities of sunspots in an active regions (Hale et

* http://solarscience.msfc.nasa.gov/images/bfly.gif

al., 1919). The axis between the two polarities is nearly toroidal (east-west direction) but has a small tilt relative to the east-west direction, with the leading polarity closer to the equator. The mean tilt angle increases from lower latitude to higher latitude (3.7° near the equator, and 10.8° at 30°–34°).

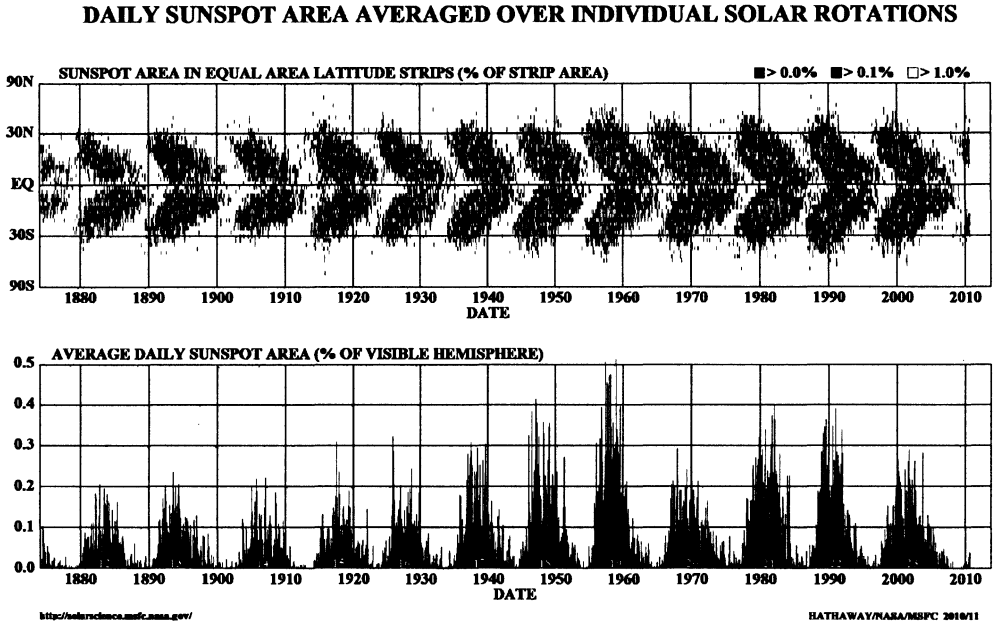

Figure 1.2 : The butterfly diagram since May 1874. The upper panel shows latitude migration in every cycle; the lower panel shows the monthly averages of the daily sunspot areas.

1.1.3 Sunspot classifications

According to the different configurations of the sunspots and sunspot groups, different classification schemes have been established, including the Mount Wilson Sunspot Magnetic Classification[†] and the *Zürich* sunspot classification (e.g. Alexander, 2009). In this thesis, we restrict our description to the Mount Wilson Sunspot

[†] http://www.spaceweather.com/glossary/magneticclasses.html

Magnetic Classification for simplicity. This was first introduced by Hale et al. in 1919, and is defined as follows.

> *α: a unipolar sunspot group.*
>
> *β: a sunspot group having both positive and negative magnetic polarities (bipolar), with a simple and distinct division between the polarities.*
>
> *γ: a complex active region in which the positive and negative polarities are so irregularly distributed as to prevent classification as a bipolar group.*
>
> *$\beta\gamma$: a sunspot group that is bipolar but which is sufficiently complex that no single, continuous line can be drawn between spots of opposite polarities.*
>
> *δ: a qualifier to magnetic classes indicating that umbrae separated by less than 2 degrees within one penumbra have opposite polarity.*
>
> *$\beta\delta$: a sunspot group of general beta magnetic classification but containing one (or more) delta spot(s).*
>
> *$\beta\gamma\delta$: a sunspot group of beta-gamma magnetic classification but containing one (or more) delta spot(s).*
>
> *$\gamma\delta$: a sunspot group of gamma magnetic classification but containing one (or more) delta spot(s).*

The magnetic class of a active region can change with time. For example, AR 9684 which produced an X1.0 flare associated with a fast coronal mass ejection (CME) on Nov.4, 2001, was reported to change from a β region to $\beta\gamma$ and at last a $\beta\gamma\delta$ region during 6 days of observation (Tian et al., 2006).

1.1.4 Rotating sunspots

Observations shows that some sunspots rotate about their center, as shown in figure 1.3. This phenomenon was first introduced by J. Evershed in 1910. The rotating sunspots in the northern hemisphere tends to show anti-clockwise rotation, while those in the southern hemisphere preferentially show clockwise rotation (Hale,

1927; Bao et al., 2002). This is generally associated with the magnetic helicity which also shows a hemispherical pattern (see later).

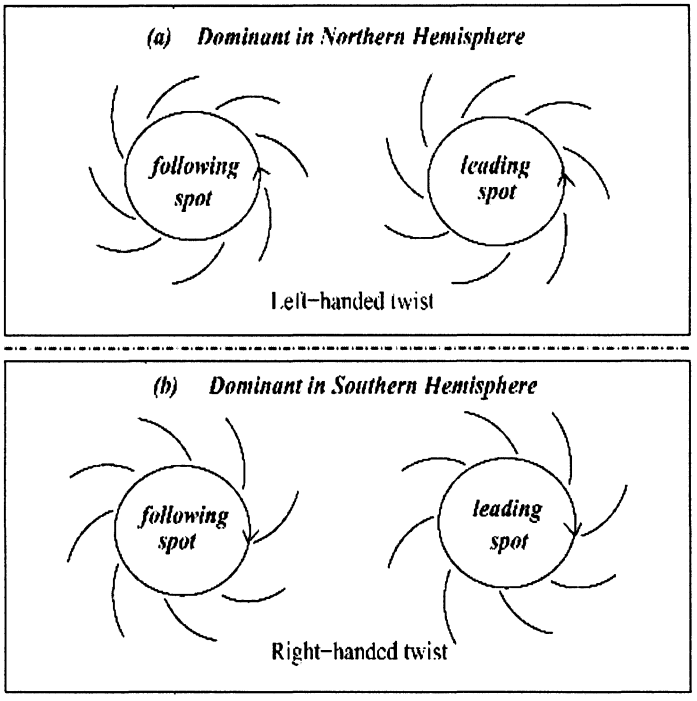

Figure 1.3 : A diagram for rotating sunspots in the northern and southern hemispheres.

With the help of high spatial and temporal resolution instruments like those on SOHO (Domingo et al., 1995) and TRACE (Handy et al., 1999), research with rotating sunspots has come to the fore in recent years. Brown et al. (2003) calculated the velocity of rotating sunspots of seven active regions using observations from the TRACE white-light channel and showed that the sunspots could rotate up to 200° during a period of 3–5 days. It was also noted that the rotating sunspots show different angular velocities with radius, with the penumbra exhibiting the fastest rotation. Brown et al. also pointed out that the method for deducing rotation in the umbra

was less accurate due to the general lack of discernible features and data points to track.

Yan et al. (2008) made a classification of observed rotating sunspots based on their directions of rotation and relative positions (i.e., in the leading or following polarity of an active region). They identified 186 rotating sunspots in 153 active regions observed by TRACE and the SOHO/Michelson Doppler Imager (MDI, see later) in solar cycle 23. 42% of the rotating sunspots were found to be spinning in only one polarity, 22% spinning in both polarities, 22% with one sunspot rotating around the other without spin.

The rotation of sunspots is thought to be related to the emergence of twisted flux tubes (e.g. Magara and Longcope, 2001). If so, the velocity of sunspot rotation is determined by the twist and emergence rate of the twisted flux tube from beneath the photosphere (Brown et al., 2003). Zhao et al. (2003) showed an observation using local helioseismology techniques that indicated that the twists often seen at the level of the photosphere also exist below the photosphere.

1.2 Magnetic Helicity

Magnetic helicity measures how much a set of magnetic flux tubes are sheared and/or wounded around each other (e.g. Berger et al., 1984). It is an important parameter in solar dynamo theory (Parker, 1955) and has been of great interest in the study of solar physics. Magnetic helicity will be defined mathematically in the next subsection. An important property of magnetic helicity is that it is approximately conserved in high magnetic Reynolds number plasmas, even in the presence of dissipative processes (Berger et al., 1984). The conservation of magnetic helicity provides a constraint on the evolution of the magnetic field, making the helicity an

important parameter in several MHD relaxation theories used to explain a range of solar phenomena, like coronal heating, flares and CMEs. It has also been postulated that accumulated magnetic helicity in the solar convection zone, below the photosphere, can lead to dynamo saturation, limiting the efficiency of the solar dynamo (Brandenburg et al., 2005; Démoulin et al., 2007).

1.2.1 Definitions

Helicity is defined via an intergal form given by $\int \mathbf{X} \cdot \nabla \times \mathbf{X}\, d^3x$ (Moreau et al., 1961). In this context, the magnetic helcity was introduced as

$$H = \int_V \mathbf{A} \cdot \mathbf{B}\, d^3x \tag{1.1}$$

where $\mathbf{A}$ is the vector potential, $\mathbf{B}$ the magnetic field strength, $\mathbf{B} = \nabla \times \mathbf{A}$ and the volume V is bounded by a magnetic surface with $B_n = \mathbf{B} \cdot \hat{\mathbf{n}} = 0$ ($\hat{\mathbf{n}}$ is the normal to the surface).

However, the boundary condition of $B_n = 0$ is not applicable for most regions of interest in solar physics, since, for example, most such regions are driven by magnetic flux that crosses the photosphere. As a result, Berger et al. (1984) introduced the *relative helicity*, which can be written as (Finn and Antonsen, 1985)

$$H = \int_V (\mathbf{A} \cdot \mathbf{B} - \mathbf{A_p} \cdot \mathbf{B_p})\, d^3x \tag{1.2}$$

Here, $\mathbf{A_p}$ is the vector potential of a reference magnetic field, $\mathbf{B_p}$ with $\mathbf{B_p} = \nabla \times \mathbf{A_p}$. The requirement is $\mathbf{A}_{p,t} = \mathbf{A}_t$, i.e., on the surface of the volume V, the vector potentials $\mathbf{A_p}$ and $\mathbf{A}$ have the same tangential components.

Observationally, the measurement of magnetic field is restricted to the photosphere and lower chromosphere. It is currently impossible to measure the magnetic field everywhere within the whole volume. However, in this thesis, since it is the

relationship of magnetic helicity injection and sunspot rotation that is under investigation, what we need is to measure the change rate of magnetic helicity injected through the photosphere.

The evolution of H inside V is (Berger, 1984)

$$\begin{aligned}\frac{dH}{dt} &= 2\int_S \mathbf{A_p}\times(\mathbf{v}\times\mathbf{B})\cdot\hat{\mathbf{n}}\,dS + \left.\frac{dH}{dt}\right|_{dis.} \\ &= \left.\frac{dH}{dt}\right|_{S_p} + \left.\frac{dH}{dt}\right|_{S_c} + \left.\frac{dH}{dt}\right|_{dis.}\end{aligned} \tag{1.3}$$

Its change is mainly due to the helicity transfer through the boundary of this volume (helicity flux) and the dissipation in the volume V. When this volume is part of solar corona, it is typically bounded below by the photosphere (S_p) and bounded above somewhere in the corona (S_c).

The helicity dissipation rate $\left.\frac{dH}{dt}\right|_{dis.}$ in Eqn.1.3 is

$$\left.\frac{dH}{dt}\right|_{dis.} = -2c\int_V \eta\mathbf{J}\cdot\mathbf{B}\,d^3x \tag{1.4}$$

However, it is negligible in all the processes occurring in the solar corona (Berger, 1984), since with a classical resistivity, the minimum dissipation time for a typical coronal structure is the order of 10^5 years.

The helicity flux through the upper boundary $\left.\frac{dH}{dt}\right|_{S_c}$ is assumed to be carried away from the Sun by CMEs (Démoulin et al., 2007).

In addition, the helicity flux through the photosphere can be calculated via (Berger et al., 1984)

$$\left.\frac{dH}{dt}\right|_{S_p} = 2\int_{S_p}[(\mathbf{A_p}\cdot\mathbf{B_t})v_n - (\mathbf{A_p}\cdot\mathbf{v_t})B_n]\,dS \tag{1.5}$$

where B_n,B_t,v_n,v_t are the tangential and normal components of $\mathbf{B}$ and $\mathbf{v}$ with respect to the photosphere. Equation 1.5 can be further simplified as

$$\left.\frac{dH}{dt}\right|_{S_p} = -2\int_{S_p}(\mathbf{A_p}\cdot\mathbf{u})B_n\,dS \tag{1.6}$$

with the velocity $\mathbf{u}$ is defined as

$$\mathbf{u} = \mathbf{v_t} - v_n \frac{\mathbf{B_t}}{B_n} \tag{1.7}$$

Here $\mathbf{u}$ is tangential to the photosphere and may be interpreted as the footpoint velocity of the flux tubes on the photosphere when the magnetic field is simply advected, i.e., a combination of the true transverse velocity $\mathbf{v_t}$ and the projected velocity from the emergence of a twisted structure $-v_n \frac{\mathbf{B_t}}{B_n}$ (Démoulin et al., 2007).

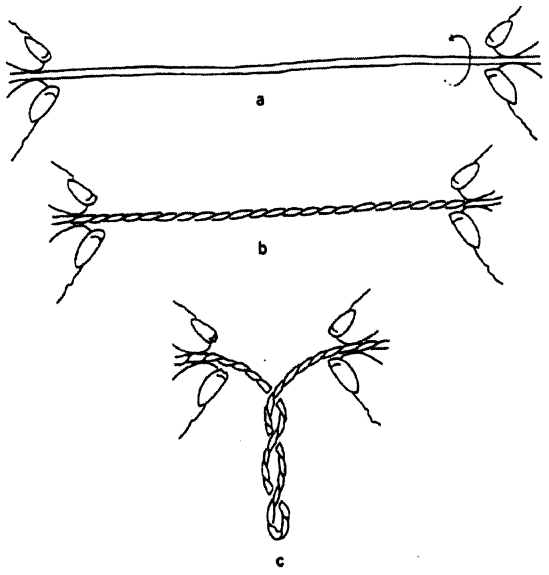

Figure 1.4 : A diagram showing the twist (b) and writhe (c).

The magnetic helicity can generally be decomposed into two terms: *twist* and *writhe*, i.e., $H = H_{tw} + H_{wr}$. Twist is due to the magnetic field line twisting around the axis of the flux tube, which can be illustrated by fixing one end of a rope, and rotating the other end (see Fig. 1.4a,b*), while writhe originates from the twist of

* http://www.bioclassification.org/papers/writhe/2004_Quine.pdf

the axis of the flux tube, as in Fig. 1.4c, resulting from the approach of the two ends of the twisted rope. As the total helicity is conserved, an increase of the writhe means a decrease of the twist.

1.2.2 Observations of magnetic helicity injection

Magnetic helicity tends to follow a common tendency called the hemispheric helicity rule (Pevtsov, 2008): solar magnetic fields in the northern (southern) hemisphere have negative (positive) sign of helicity. Typically, about $70 - 80\%$ of active regions follow this hemispherical rule. Several phenomena in the solar atmosphere display this pattern. For example, the sunspot whorls (spiral pattern of chromospheric fibrils), "magnetic tongues" in emerging active regions, and soft X-ray sigmoids (Démoulin et al., 2007). Many mechanisms have been considered to explain this tendency, including solar differential rotation, the Coriolis force due to solar rotation, solar dynamo and turbulent convection in the upper convection zone (known as Σ effect).

Démoulin (2007) reviews recent theoretical and observational relations between the magnetic helicity injection and a variety of solar phenomena. Nindos et al. (2004) found that the magnetic helicity in active regions that exhibits CMEs is much larger than those that produce just confined flares, and that confined flares occur more often in active regions with mixed sign of α (a spatial-varying function satisfying $\nabla \times \mathbf{B} = \alpha(\mathbf{r})\mathbf{B}$ when the magnetic field is force-free), indicating a possible relation to the mixed sign of helicity. Démoulin suggested that this result may be confirmed by mapping out the of *magnetic helicity density* (the spatial distribution of magnetic helicity flux, see later).

Another interesting result is the asymmetry of helicity injection in emerging active regions (Tian and Alexander, 2009). They made a statistical study of 15 active regions

and calculated the helicity injection into the leading and following polarities. They found the amount of helicity injected into the leading polarity was several times (typically 3–10 times) larger than that of following polarity. The authors suggested that this mainly resulted from the different speeds of emergence between the two polarities. This has been borne out by a numerical simulation (Fan et al., 2009).

1.3 Instruments

The data used in this thesis mainly comes from SOHO and TRACE, both of which will be given a brief introduction in the following.

1.3.1 SOHO spacecraft

SOHO (the Solar and Heliospheric Observatory) is a project of international cooperation between ESA and NASA. It was designed to answer some fundamental questions about the deep core of the sun, the outer corona, and the solar wind (Domingo et al., 1995). SOHO was launched by NASA on Dec. 2, 1995. It orbits around the First Lagrangian Point (L1), where it is kept by the combined gravity of the Earth and Sun. The L1 point is approximately 1.5 million kilometres away from Earth in the direction of the Sun, so that SOHO can have an uninterrupted view of the sun.

SOHO has 12 complementary instruments onboard, including the Michelson Doppler Imager (MDI), the Extreme ultraviolet Imaging Telescope (EIT), and the Large Angle and Spectrometric Coronograph (LASCO). MDI can measure the longitudinal component of the Sun's magnetic field on the photosphere. EIT provides information on the evolution of chromospheric and coronal structures. LASCO is a white light coronagraph that can be used to observe CMEs between 1.1 to 30 $R_{\odot}$.

1.3.2 TRACE spacecraft

TRACE (Transition Region and Coronal Explorer) images the solar corona and transition region at high angular and temporal resolution. It was launched in April 1998, scheduled to allow joint observations with SOHO during the rising phase of the solar cycle.

The telescope on TRACE has a field view of $8.5' \times 8.5'$ (compared to $R_\odot \sim 16'$) and its spatial resolution is $1''$. It can detect three EUV wavelengths, four UV wavelengths, and a white-light channel, observing plasma with temperature from 6×10^3K to 1×10^7K (Handy et al., 1999), as shown in table 1.1.

Table 1.1 : TRACE passbands (from Handy et al., 1999).

Wavelength (Å)	Emission	Bandwidth (Å)	Temperature (K)
171	Fe IX/X	6.4	$1.6 - 2.0 \times 10^5$
195	Fe XII/XXIV	6.5	$5.0 - 20 \times 10^5$, $1.1 - 2.6 \times 10^7$
284	Fe XV	10.7	$1.25 - 4.0 \times 10^6$
1216	H I Ly α	84	$1.0 - 3.0 \times 10^4$
1550	C IV	30	$6.0 - 25 \times 10^4$
1600	UV Cont, C I, Fe II	275	$4.0 - 10 \times 10^3$
1700	Continuum	200	$4.0 - 10 \times 10^3$
5000	White Light	broad	$4.0 - 6.4 \times 10^3$

1.4 Outline of this thesis

This thesis aims to present observations of helicity injection and the associated velocity characteristics of rotating sunspots. The flow velocity field in and around sunspots is an important parameter for the calculations in this thesis. Consequently, Chapter 2 provides a brief description of four flow velocity inversion techniques, in-

cluding the local correlation tracking method (LCT), the Differential Affine Velocity Estimator (DAVE), the minimum energy fit technique (MEF), and the modified DAVE method for vector magnetograms (DAVE4VM). Based on the comparisons of these techniques, the DAVE method is chosen in our analysis, and the calculation of helicity injection rate based on this method is also reviewed in Chapter 2.

Chapter 3 provides observations on four active regions which contain typical rotating sunspots. The results from our calculations present a determination of the injection of magnetic helicity through the photosphere. With the accumulation of helicity in the solar corona, the active region structures display sigmoid (S-shaped) features or eruptive activities like CMEs and flares. Possible explanations relating theses solar phenomena to the helicity accumulation are also discussed.

Sunspot rotation and its underlying physical processes are of primary interest and Chapter 4 is devoted to providing the calculations on the rotation speeds and their relation to the emergence of the active region. In addition, results on the interesting phenomenon of counter-rotating sunspots are presented in this chapter.

A summary is given in Chapter 5, and some perspective studies are discussed to conclude the thesis.

Chapter 2

Determining the velocity of rotating sunspots and the associated injection of magnetic helicity

This chapter is constructed with two sections. The first section mainly focuses on the introduction of the available velocity inversion techniques. The second section talks about the methods used for determining the angular velocity of rotating sunspots, including the DAVE method using magnetogram data and the method of Brown et al. (2003) using intensity data from the TRACE white light channel.

2.1 Methods to calculate magnetic helicity injection

The evolutions of CMEs and solar flares are thought to be related to the magnetic helicity injection through the photosphere (e.g. Hood and Priest, 1979). In order to determine the helicity injection rate, the plasma velocity on the photosphere is required in association with the magnetic field measurements (see eqn. 1.6, 1.7). Several methods have been introduced to accomplish this goal, including the local correlation tracking method (LCT, Leese et al., 1970), the Differential Affine Velocity Estimator (DAVE, Schuck, 2006) for line-of-sight (los) magnetograms, minimum energy fit technique (MEF, Longcope, 2004), and the modified DAVE method for vector magnetograms (DAVE4VM, Schuck, 2008) for vector magnetograms.

2.1.1 Velocity inversion techniques: LCT, DAVE, MEF, DAVE4VM

The LCT method was developed by Leese et al. (1970) to track clouds in the Earth's atmosphere, and introduced to solar physics for the measurement of the optical flow on a series of observations of solar granulation (November and Simon, 1988). With the LCT method, the horizontal motion of magnetic field line footpoints in active regions was inferred by Chae (2001) from a sequence of los magnetograms.

In order to correlate images at different times, a series of magnetograms are aligned based on the angular velocity of solar differential rotation, which is given by Howard et al (1990), as

$$\omega = 2.894 - 0.428 \sin^2 \phi - 0.370 \sin^4 \phi \ \ \mu rad\, s^{-1} \tag{2.1}$$

where ϕ is the solar latitude. In other words, successive magnetograms are derotated to a singe reference time.

For two successive magnetograms with intensity of $I(\mathbf{x}, \tau)$ and $I(\mathbf{x}, \tau + \Delta t)$, the degree of similarity between two subregions can be calculated from their correlation function (e.g. Schuck, 2006)

$$C(\chi, \mathbf{u}, \tau) = \int W(\mathbf{x} - \chi)[I(\mathbf{x}, \tau + \Delta t) - I(\mathbf{x} - \mathbf{u}\Delta t, \tau)]^2 \, d^2\mathbf{x} \tag{2.2}$$

where $\mathbf{u}$ is the local velocity, which is chosen by minimizing eqn. 2.2, $W(\mathbf{x})$ is a window function, typically a two-dimensional Gaussion function, localizing the two subregions, and Δt is the time difference between two successive images.

The next task is to determine the vector potential of the potential reference field $\mathbf{A_p}$ from the magnetic field distribution on the photosphere satisfying

$$\nabla \times \mathbf{A_p} \cdot \hat{\mathbf{n}} = B_n, \quad \nabla \cdot \mathbf{A_p} = 0, \quad \mathbf{A_p} \cdot \hat{\mathbf{n}} = 0 \tag{2.3}$$

Using a discrete Fourier transform $F(T) = \sum_{x,y} T(x,y)e^{-ik_x x - ik_y y}$, the horizontal components of $\mathbf{A_p}$ can be derived from B_n, as,

$$\mathbf{A}_{p,x} = F^{-1}\left[\frac{ik_y}{{k_x}^2 + {k_y}^2} F(B_n)\right]$$
$$\mathbf{A}_{p,y} = F^{-1}\left[\frac{-ik_x}{{k_x}^2 + {k_y}^2} F(B_n)\right] \tag{2.4}$$

The helicity injection rate can now be calculated using eqn. 1.6 with the derived $\mathbf{u}$ and $\mathbf{A_p}$. Chae et al. (2001) calculated the helicity injection rate in AR 8668 with this method and found it was an order of magnitude higher than that due to the solar differential rotation, indicating that some other transverse flows are present or alternatively that the field emerges with significant twist.

The LCT method is limited in that it assumes that the velocity is constant at a certain position and does not have any contraction, dilation or rotation of the magnetic field. In order to incorporate such motions Schuck (2006) developed the Differential Affine Velocity Estimator (DAVE) in which an affine flow of the form,

$$\mathbf{u}_\chi(\mathbf{x}) = (U_0, V_0) + \mathbf{W} \cdot (\mathbf{x} - \chi) \tag{2.5}$$

is used where

$$\mathbf{W} = \nabla \mathbf{u}(\mathbf{x}) \mid_{\mathbf{x}=\chi} = \begin{pmatrix} U_x & U_y \\ V_x & V_y \end{pmatrix} \tag{2.6}$$

The correlation function for the DAVE method becomes

$$C(\chi, \mathbf{u}, \tau) = \int W(\mathbf{x} - \chi)[I(\mathbf{x}, \tau + \Delta t) - e^{-(U_x + V_y)\Delta t} I(\mathbf{x} - \mathbf{u}\Delta t, \tau)]^2 \, d^2\mathbf{x} \tag{2.7}$$

For the minimization of this correlation equation, the vector parameters describing the flow $(U_0, V_0, U_x, V_y, U_y, V_x)$ can be achieved. The DAVE method is regarded as the most robust of the available techniques and will be used in our calculations to be described in subsequent chapters.

The minimum energy fit technique (MEF) was introduced to infer the photospheric velocity from a series of vector magnetograms (Longcope, 2004). It begins with the vertical component of the induction equation,

$$\nabla_h \cdot (v_z \mathbf{B}_h - B_z \mathbf{v}_h) = \frac{\partial B_z}{\partial t} \tag{2.8}$$

where subscript 'h' denotes the horizontal component, and 'z' denotes the vertical component. Two scalar potentials ϕ and ψ are introduced to solve the above equation,

$$v_z \mathbf{B}_h - B_z \mathbf{v}_h = \nabla_h \phi + \nabla_h \psi \times \hat{z} \tag{2.9}$$

ϕ can be solved from eqn. 2.8 and eqn. 2.9. In order to get an unique velocity field, another constraint with the following minimization is provided.

$$T(\psi, v_z) = \frac{1}{2} \int_M (|\mathbf{v}_h - \mathbf{u}_h|^2 + |v_z - u_z|^2)\, dx\, dy \tag{2.10}$$

ψ and v_z in this functional are solved with standard Jacobi relaxation until the smallest possible energy T can be found. Then the horizontal velocity $\mathbf{v}_h$ can be obtained from eqn. 2.9, that is

$$\mathbf{v}_h = \frac{1}{B_z}(v_z \mathbf{B}_h - \nabla_h \phi - \nabla_h \psi \times \hat{z}) \tag{2.11}$$

An advantage of MEF is that it can incorporate velocity information from other measurement methods, for example, Doppler velocity and LCT (Ravindra et al, 2008). The Doppler velocity is used as an independent constraint on the vertical velocity u_z, while the LCT velocity used to constrain the horizontal velocity $\mathbf{u}_h$. They tested this method with different constrained versions of MEF, and found that MEF+LCT+u_z works better on the flow field than other versions (e.g., MEF+LCT or MEF+u_z). Another advantage of MEF is that the velocity is derived from the ideal induction

equation and it is suitable for a boundary condition in simulations of flux emergence (Longcope, 2004).

Schuck (2008) modified the DAVE method to DAVE4VM (the suffix '4VM' denoting that it is for vector magnetic fields), producing a velocity estimator for the vector magnetograms. With the horizontal component of the magnetic filed incorporated, the three dimensional velocity has the form of,

$$\mathbf{v}(\mathbf{x}) = \begin{pmatrix} u_0 \\ v_0 \\ w_0 \end{pmatrix} + \begin{pmatrix} u_x & u_y \\ v_x & v_y \\ w_x & w_y \end{pmatrix} \begin{pmatrix} x \\ y \end{pmatrix} \tag{2.12}$$

Then with the minimization of the error metric C, the velocity can be derived.

$$C = \int W(\mathbf{x}-\chi, t-\tau)\{\partial_t B_z(\mathbf{x},t) + \nabla_h \cdot [B_z(\mathbf{x},t)\mathbf{v}_h(\mathbf{x}-\chi) - v_z(x-\chi)\mathbf{B}_h(\mathbf{x},t)]\}^2 \, dt \, dx^2 \tag{2.13}$$

A brief comparison of the four methods is shown in table 2.1. Because of the better accuracy of the DAVE method (Welsch et al., 2007) and the limited availability of vector magnetic field observations, the DAVE method will be applied throughout this thesis.

Table 2.1 : Comparisons of the velocity inversion techniques

	LCT	DAVE	MEF	DAVE4VM
magnetogram	los	los	vector	vector
induction eqn.	not satisfied	statistically satisfied	satisfied	statistically satisfied

2.1.2 Helicity flux calculation with DAVE

The integrand in eqn. 1.6 is called the helicity flux density, $G_A(\mathbf{x})$, with $G_A(\mathbf{x}) = -2(\mathbf{A}_p \cdot \mathbf{u})B_n$. However, it has been shown that this quantity is subject to the presence of fake polarities which severely hinder the accuracy of the helicity calculations (Demoulin, 2007). To resolve this issue, a new helicity flux density parameter, G_θ, was introduced by Pariat et al. (2005):

$$G_\theta(\mathbf{x}_i) = -\frac{B_{n,i}}{2\pi}\int_{s'}\frac{[(\mathbf{x}-\mathbf{x}')\times(\mathbf{u}-\mathbf{u}')]_n}{\mid \mathbf{x}-\mathbf{x}' \mid^2}B'_n\, dS' \tag{2.14}$$

G_θ can be split into two components, G_i^S and G_i^M (Chae 2007), i.e.,

$$G_\theta(\mathbf{x}_i) = G_i^S + G_i^M \tag{2.15}$$

where G_i^S is the self helicity (when $\mathbf{x} = \mathbf{x}'$ in eqn. 2.14), and G_i^M is the mutual helicity (when $\mathbf{x} \neq \mathbf{x}'$ in eqn. 2.14). With the velocity field derived from the DAVE method (eqn. 2.6), these quantities can be written as,

$$G_i^S \approx -\frac{B_i^2}{4\pi}\Delta S \cdot (V_{x,i} - U_{y,i}) \tag{2.16}$$

$$G_i^M = -\frac{B_i}{2\pi}\Delta S\left[V_i(f*B)_i - (f*VB)_i - U_i(g*B)_i + (g*UB)_i\right] \tag{2.17}$$

where '$*$' donates the convolution operation. f and g have the forms of,

$$f(x,y) = \begin{cases} \dfrac{x}{x^2+y^2} & \text{if } x^2+y^2 \neq 0 \\ 0 & \text{if } x^2+y^2 = 0 \end{cases} \tag{2.18}$$

$$g(x,y) = \begin{cases} \dfrac{y}{x^2+y^2} & \text{if } x^2+y^2 \neq 0 \\ 0 & \text{if } x^2+y^2 = 0 \end{cases} \tag{2.19}$$

G_i^M can be achieved much faster by applying a Fast Fourier transform for the convolutions in eqn. 2.17. With the integral of G_θ, the helicity injection rate can then be readily determined, via

$$\frac{dH}{dt} = \int G_\theta \, dS \tag{2.20}$$

2.2 Methods for measuring the velocity of rotating sunspots

2.2.1 DAVE with MDI magnetograms

It has been shown that the DAVE method can be used to track the magnitude and directions more accurately than other available methods (Welsch et al., 2007). The line-of-sight (los) magnetograms have been recorded routinely by SOHO since 1996. As a result, the DAVE method is an ideal technique for calculating the rotating speed of the sunspots over the course of the SOHO mission.

Before the los magnetograms can be analysed with this method, they are first derotated and aligned using eqn. 2.1. Then the velocities at each pixel are derived from two successive magnetograms, typically separated by 96 minutes. Another important procedure is to find the centers of the sunspots about which they are presumed to rotate. This can be done by using the weighted average of each pixel in the sunspot region of interest.

Having obtained the velocity profile in the sunspot region and the position of its center, the rotation velocity can be derived by an average of the velocities in each pixel with a fixed $|\mathbf{r}|$ around the center. However, $|\mathbf{r}|$ cannot be chosen too small, for example, $|\mathbf{r}| = 2$ pixels, since this would make the perimeter, $l = 2\pi|\mathbf{r}| \approx 13$ pixels, too small to accurately derive the velocity of the rotating sunspots. As a result, when we choose rotating sunspot samples, the sunspot should be large enough to provide

enough pixels for inclusion into the averaging procedure. This provides a restriction on the sample of rotating sunspots.

2.2.2 Brown et al. with TRACE white light channel

Before the DAVE method was presented by Schuck (2006), a method was demonstrated by Brown et al. (2003) to determine the rotating velocity of sunspots. A series of photospheric white-light images with high spatial and temporal resolution were selected for each sunspot in the study. After determining the center of the sunspot and extracting time-slices at a chosen radius, the new angle-time plot (a 'stackplot') is constructed for each sunspot. Then the rotation of the sunspot can be measured from the slopes of the 'diagonal streaks', as shown in Fig. 2.1.

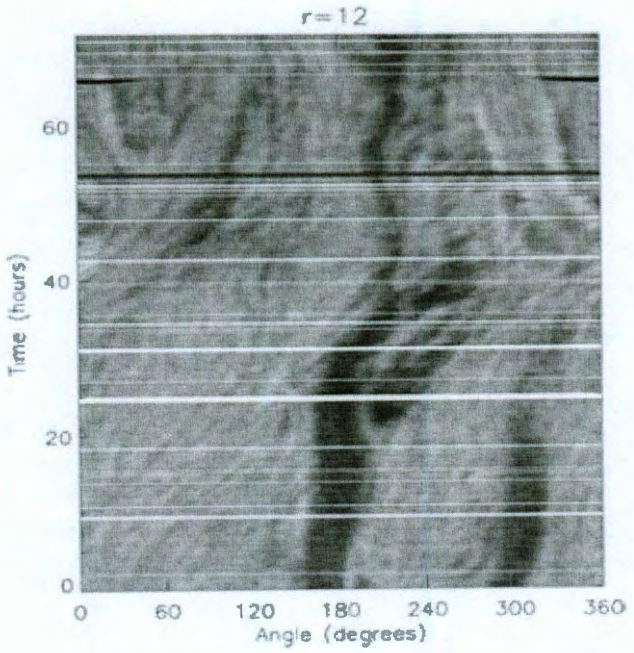

Figure 2.1 : A diagram for the rotation velocity determination from time-slice method of Brown et al. (2003).

With this method, Brown et al. (2003) calculated the velocity of rotating sunspots of seven active regions and showed that the sunspots could rotate up to 200° during a period of 3–5 days. In addition, the rotating sunspots show different angular velocities with radius, with the penumbra exhibiting the fastest rotation.

Compared to the method described above, one advantage of the DAVE method is that it can provide the full velocity field on the photosphere, not just the angular velocity. Another one is that it can be directly applied to the los magnetograms from SOHO, which has provided observations of the sun for 3 years longer than TRACE and has a greater field view, providing more rotating sunspot examples. Moreover, it also ties more directly to the magnetic helicity calculation.

Chapter 3

Magnetic helicity injection by rotating sunspots

3.1 Introduction

The rotation of sunspots can be decomposed into two parts: in situ rotation and the motion of one sunspot region around another, both of which can contribute to injection of magnetic helicity through the photosphere (Longcope et al., 2007). As the magnetic helicity accumulates, coronal loops related to this active region can display energized structures like sigmoids (e.g. Alexander, 2006; Gibson et al., 2004), solar flares and CMEs (Forbes, 2000; Nandy, 2008). One important driver mechanism for CMEs and filament eruptions is thought to be the kink instability, due to the twist of magnetic flux tube exceeding some critical value. For example, Hood and Priest (1979) analysed flux tubes under different conditions and found the critical twist is 3.3π (1.65 turns) for the force-free field of uniform twist and typically between 2π and 6π for other fields (see also Gilbert et al., 2007).

Knowledge of the source regions of CMEs is required for the study of the relations between CMEs and active regions. Webb et al. (1987) found that 68% of CMEs are associated with eruptive prominences, 47% with X-ray events, and 37% with $H\alpha$ flares. Canfield et al. (1999) suggested that CMEs often had source regions with sigmoid structures. Subramanian et al. (2001) identified 32 events and provided the source regions of these CMEs. The criterion used in that paper include the following features: flares, plasma/material motions, EIT waves and eruption of prominences.

There are 86 flare related CMEs identified originating from 55 solar active regions between 1997 to 2005 (Guo et al., 2007). Wang et al. (2008) presented source regions of 57 of the fastest ($> 1500 km/s$) CMEs from 1996 to 2007, and showed a general trend between the size of an active region and the likelihood of its producing a fast CME.

In this chapter, observations of 4 active regions with rotating sunspots are shown in section 3.2, with magnetic helicity injection and other related solar phenomena provided. In section 3.3, we present our preliminary work on the relation of magnetic helicity injection and solar flare productivity of the active regions. Finally, a summary is given in section 3.4.

3.2 Case studies of four active regions

3.2.1 AR 9114

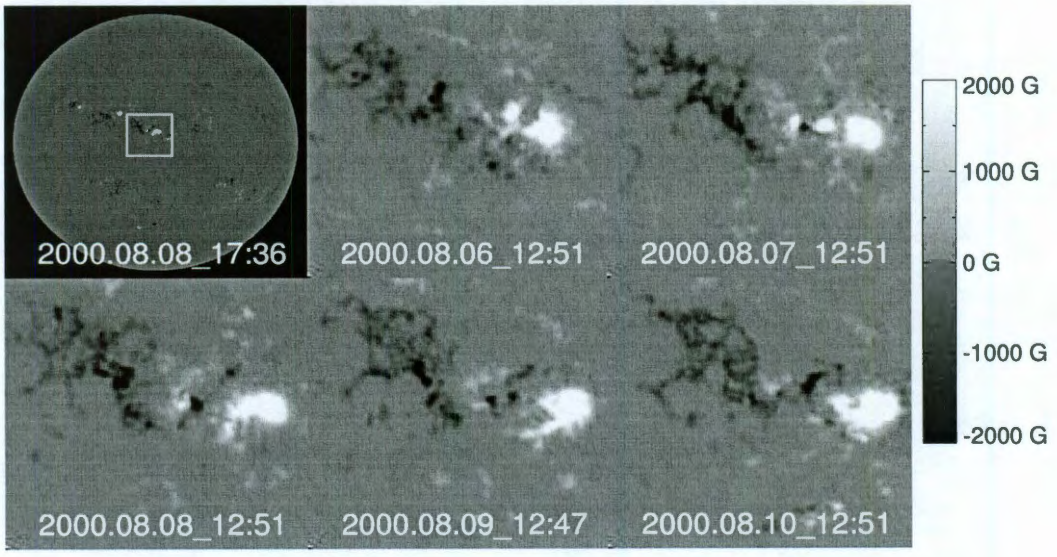

Figure 3.1 : SOHO/MDI observations of AR 9114.

Table 3.1 : Location and magnetic class of AR 9114.

Date	Position	Area	magnetic type
2000 Aug. 6	N12E41	230	β
2000 Aug. 7	N12E28	250	β
2000 Aug. 8	N12E14	160	$\beta\gamma$
2000 Aug. 9	N11W01	290	$\beta\gamma$
2000 Aug. 10	N11W16	290	$\beta\gamma$

AR 9114 is a typical active region with a rotating sunspot observed in the northern hemisphere (Brown et al., 2003). Its magnetic evolution is shown in Fig. 3.1. It appeared on the east limb on August 3, 2000, and arrived near the central meridian of the solar disk on August 8. This active region was a β type before Aug. 8, after when it became a $\beta\gamma$ region.

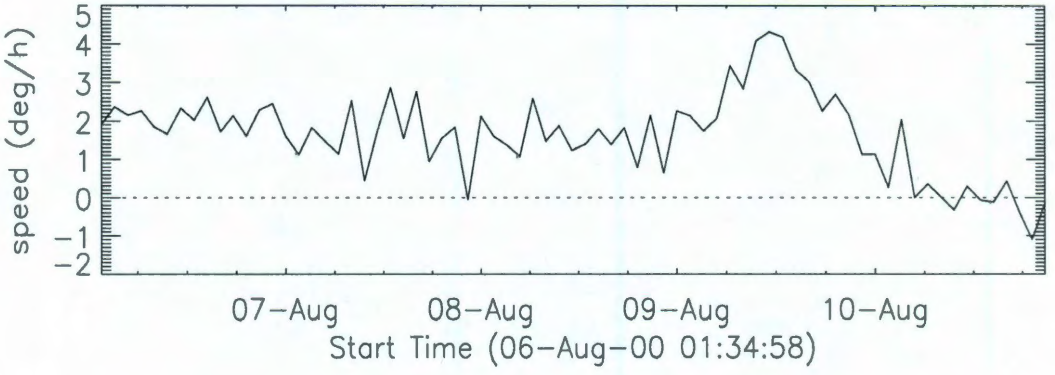

Figure 3.2 : The rotating velocity of the sunspot in positive polarity of AR 9114.

In active region 9114, the leading positive polarity is compact with strong magnetic field, while the following negative polarity has fragmented appearance. During the period of Aug. 6 to Aug. 10, the total rotation of the leading polarity is about 180° (Fig. 3.2, or Brown et al. 2003). The maximum of the angular speed is about $4°/h$,

corresponding to a velocity 0.13 km/s. After Aug. 9, the rotation slows down to a small value hard to be detected.

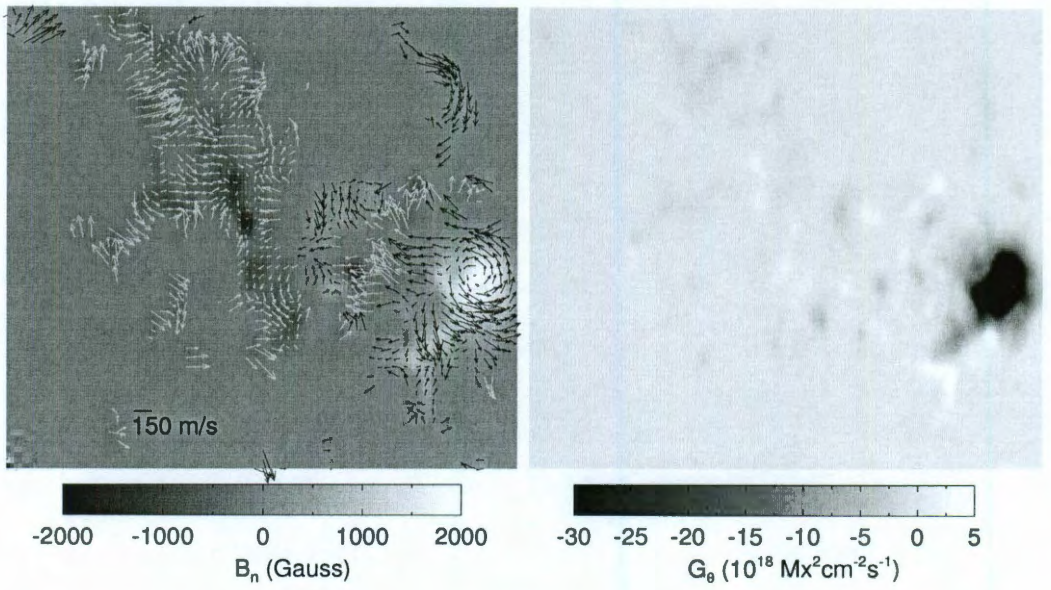

Figure 3.3 : left: Map of velocity superposed on the gray-scale map of B_n. Right: Gray-scale map of magnetic helicity flux density G_θ at 08:03, Aug. 9, 2000.

The leading polarity shows an anti-clockwise rotation. Take the observation at 08:03 Aug. 9 (Fig. 3.3) as an example. In the left panel, the gray-scale map indicates the normal component of the magnetic field, B_n, with the map of tangential velocity superposed on it. The dark regions denote the negative magnetic fields, and the white regions denote positive magnetic fields. In order to see the velocity clearly, those parts with $|B_n|$ less than $60G$ have been omitted. The arrows show the direction, while the length of the arrows indicate the amplitude of the velocity. From the left panel, a strong anti-clockwise rotation is evident in the positive polarity. The right panel in Fig. 3.3 shows the map of magnetic helicity flux density G_θ at the same time. The dark regions denote negative helicity flux density. The domination of

the negative helicity injection can be seen from this map. This location of negative helicity injection corresponds to the anti-clockwise rotation of the leading polarity.

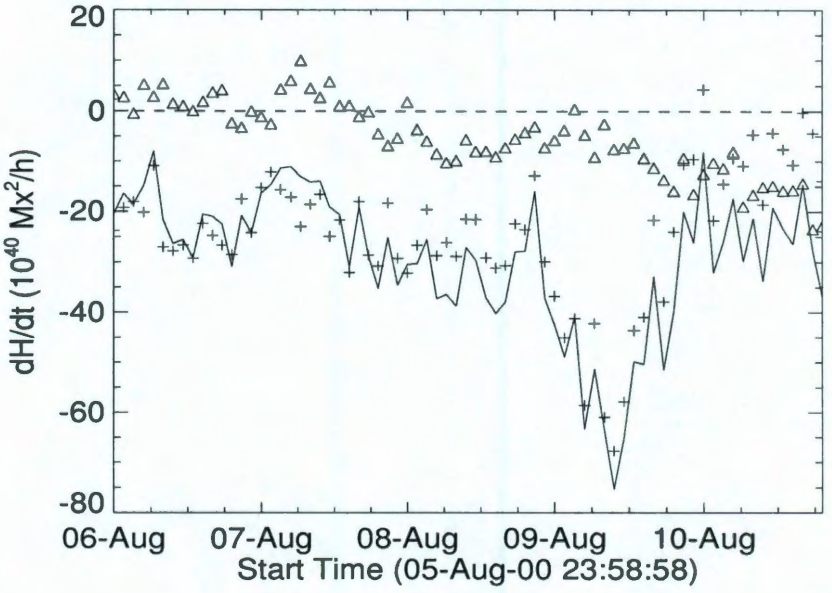

Figure 3.4 : Magnetic helcity injection rate of AR 9114 during Aug. 6 to Aug. 10, 2000. + for magnetic helicity rate through positive polarity, △ for those through negative polarity. The solid line is the total helicity injection rate.

The magnetic helicity injection rate during the five-day observations is illustrated in Fig. 3.4. First of all, an asymmetry of the helicity injection (Tian and Alexander, 2009) can be seen in AR 9114. Specifically, the magnitude of magnetic helcity injection rate through the negative polarities dH_-/dt (△ in the figure) is about $-5 \times 10^{40} Mx^2/h$, significantly smaller than the injection through the positive polarities dH_+/dt of about $-2.4 \times 10^{41} Mx^2/h$ (+ sign in the figure). This results in a total negative helicity injection of about $-3.4 \times 10^{43} Mx^2$ through the photosphere to the upper solar atmosphere. Moreover, dH_+/dt has a peak of $-7 \times 10^{43} Mx^2/h$ during Aug. 9, 2000, corresponding to the period when the leading sunspot rotates with its

maximum angular velocity (see Fig. 3.2).

(a) Aug. 7 02:04UT (b) Aug. 9 12:28UT (c) Aug. 9 21:58UT

Figure 3.5 : Inversed-S sigmoid formed as negative helicity accumulates, observed by SXT/Yohkoh.

As a result of the total negative helicity injected through the photosphere, an inverse-S shaped sigmoid is observed to form in the solar corona, seen by Yohkoh/SXT, as shown in Fig. 3.5. This phenomenon has been confirmed with simulations (e.g. Gibson and Fan et al. (2004). Fig. 3.6 shows the X-ray flux during the period of AR 9114 crossing the solar disk. The shaded regions denote the times of flares in AR 9114. Among these, a C2.3 class flare was observed between 15:33 and 17:00 UT, Aug. 9 2000. There was a halo CME associated with this event, that first appeared at 16:30 UT (Guo et al., 2007; Nindos et al., 2003), denoted by a vertical dashed line in Fig. 3.6.

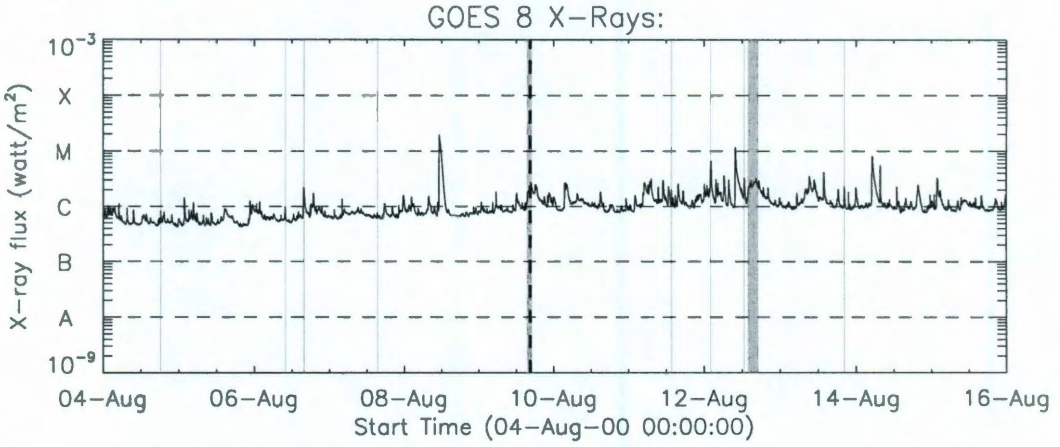

Figure 3.6 : Soft X-ray flux from Aug. 4 to Aug. 15, 2000.

As the halo CME propagates through interplanetary space, it was observed as a magnetic cloud by the WIND spacecraft (Lepping et al., 1995) at about 1 AU, near the Earth. Nindos et al. (2003) estimated the magnetic helicity of this magnetic cloud to be $(-4.76 to -19.0) \times 10^{42} Mx^2$, which is less than the amount of total helicity injection ($-3.4 \times 10^{43} Mx^2$), meaning that the total helicity from AR 9114 is large enough to drive this halo CME.

3.2.2 AR 10696

AR 10696 is a strong active region containing rotating sunspots. It appeared at the east limb on Nov. 3, 2004, located in the northern hemisphere with a low latitude of about 10°. The magnetic evolution of this active region can be seen in Fig. 3.7 and Table 3.2. It was β type with small area on Nov. 3. As it emerged through the photosphere, the area increased rapidly and its magnetic geometry developed into $\beta\gamma\delta$. The counter-clockwise rotation of the negative polarity can be seen from Fig. 3.7. After Nov. 7, it began to decay, but maintained a long east-west neutral line

with strong gradient, as reported by Big Bear Solar Observatory (BBSO).

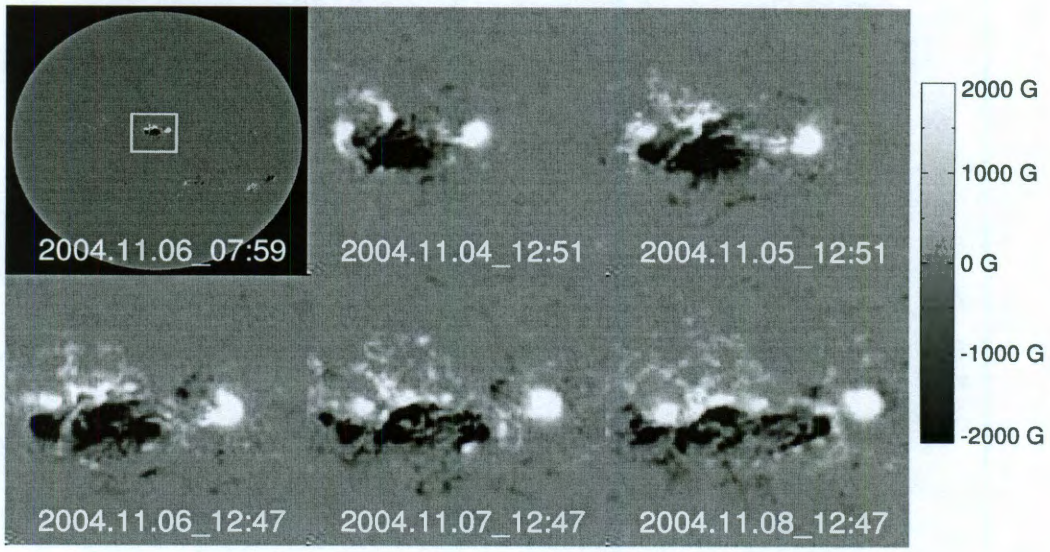

Figure 3.7 : MDI observations of AR 10696.

Table 3.2 : Location and magnetic class of AR 10696.

Date	Position	Area	magnetic type
2004 Nov. 3	N08E47	110	β
2004 Nov. 4	N12E28	270	$\beta\gamma$
2004 Nov. 5	N09E19	580	$\beta\gamma\delta$
2004 Nov. 6	N09E06	820	$\beta\gamma\delta$
2004 Nov. 7	N09W08	910	$\beta\gamma\delta$
2004 Nov. 8	N08W22	650	$\beta\gamma\delta$

During Nov. 4 to Nov. 6, the negative polarity is compact, while the positive polarity is distributed (see Fig. 3.7). Fig. 3.8 illustrates the tangential velocity of the magnetic elements (on the left) and the magnetic helicity density at 14:27 UT, Nov.

4. The magnetic elements in the negative polarity (dark region in the figure on the left) are rotating around the center in the counter-clockwise direction as the center moves toward to the west (right). The counter-clockwise rotation of the compact negative polarity contributes a large amount of negative helicity injection at this time. Moreover, the motion of the positive polarity also added negative helicity into the upper atmosphere (dark region on the right of map of helicity flux density).

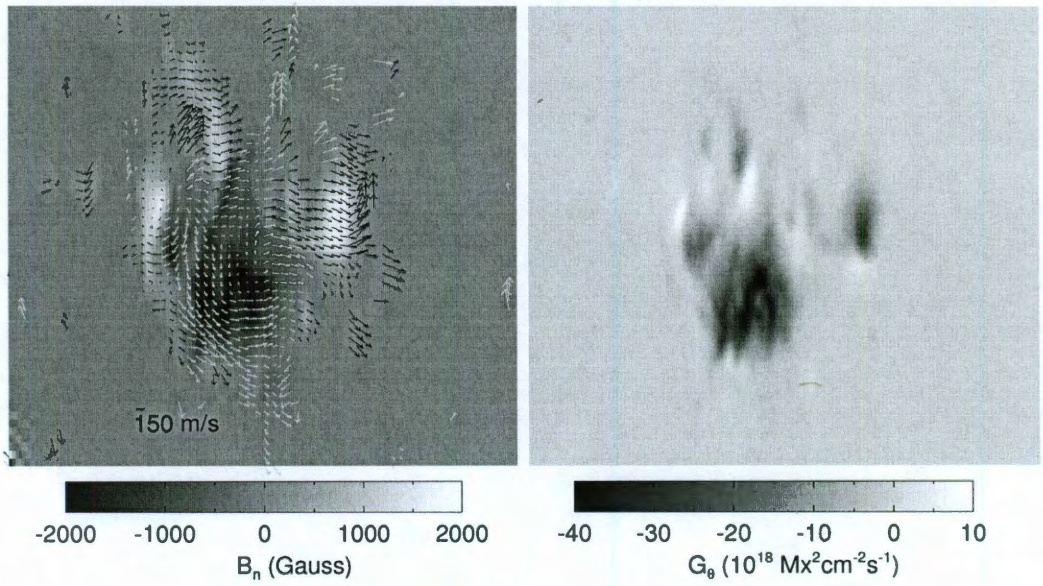

Figure 3.8 : left: Map of velocity superposed on the gray-scale map of B_n. Right: Gray-scale map of magnetic helicity flux density G_θ at 14:27, Nov.4.

The total amount of the helicity injection is about $-6.3 \times 10^{43} Mx^2$ during these 5 days. dH_+/dt is less than $-2 \times 10^{41} Mx^2/h$ for most of the time, while dH_-/dt usually exceeds $-8 \times 10^{41} Mx^2/h$ for 3 days from Nov.4 to Nov. 7, which results in the asymmetry of the helicity injection (Fig. 3.9). The injection of massive negative helicity into the north hemisphere obeys the hemispheric helicity rule (e.g. Pevtsov, 2007).

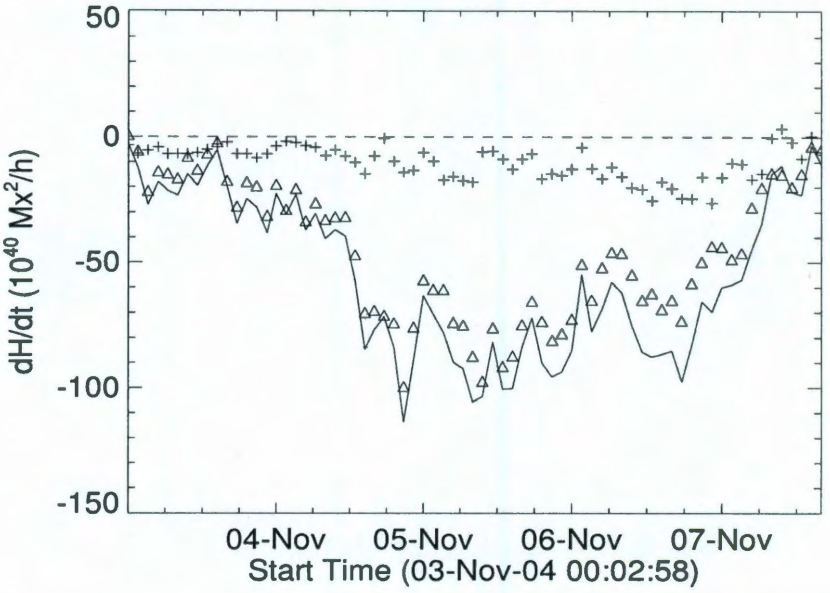

Figure 3.9 : Magnetic helcity injection rate of AR 10696 during Nov. 3 to Nov. 7, 2004. + for magnetic helicity rate through positive polarity, △ for those through negative polarity. The solid line is the total helicity injection rate.

AR 10696 was quite an active source of many strong flares and CMEs (Fig. 3.10). Three halo CMEs with velocities greater than $1500 km/s$ are reported to originate from this active region (e.g. Wang et al., 2008; denoted by the vertical dashed lines in Fig. 3.10). These fast CMEs and their related flares are listed in Table 3.3. For example, on Nov. 7, 2004, a X2.0 flare occurs between 15:42 UT and 16:15 UT, and a halo CME with velocity of 1759 km/s was observed at 16:54 UT.

Table 3.3 : Fast halo CMEs and associated flares from AR 10696.

Date	F_{start}	F_{end}	position	F_{class}	T_{CME}	$v_{CME}(km/s)$
2004-11-07	15:42:00	16:15:00	N09W17	X2.0	16:54:05	1759
2004-11-09	16:59:00	17:32:00	N08W51	M8.9	17:26:06	2000
2004-11-10	01:59:00	02:20:00	N09W49	X2.5	02:26:05	3387

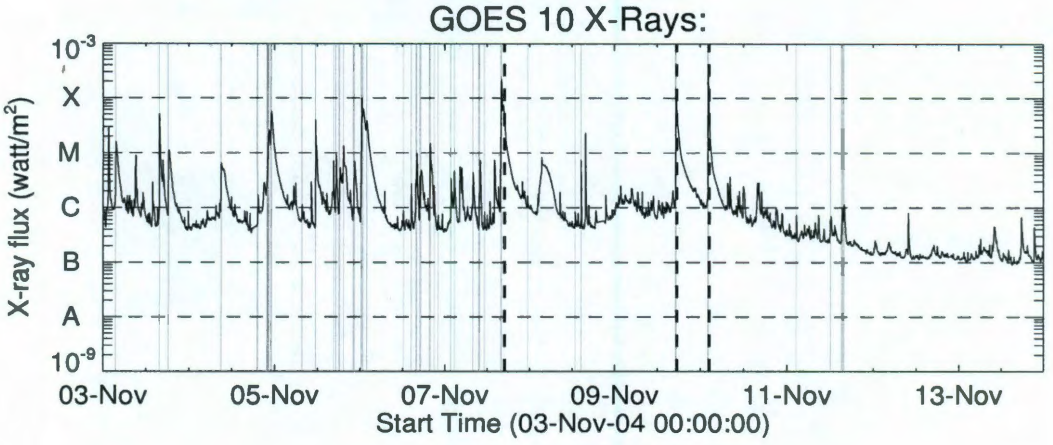

Figure 3.10 : Soft X-ray flux from Nov. 3 to Nov. 13, 2004.

(a) (b) (c)

Figure 3.11 : The evolution of a kinked filament in AR 10696 observed by TRACE 1600Å on Nov. 10, 2004, shown in the square box.

Williams et al. (2005) studied the halo CME which is accompanied by a X2.5 flare on Nov. 10, 2004. They suggested that this CME resulted from the release of a previously confined filament; and the driver of its expansion is most probably the kink instability. The evolution of this filament is shown in Fig. 3.11. The configuration of this kinked filament shows a correspondence to the total negative helicity injection of

AR 10696. In order to better qualify the relation of this halo CME and the magnetic helicity injection, further work is needed.

3.2.3 AR 9906

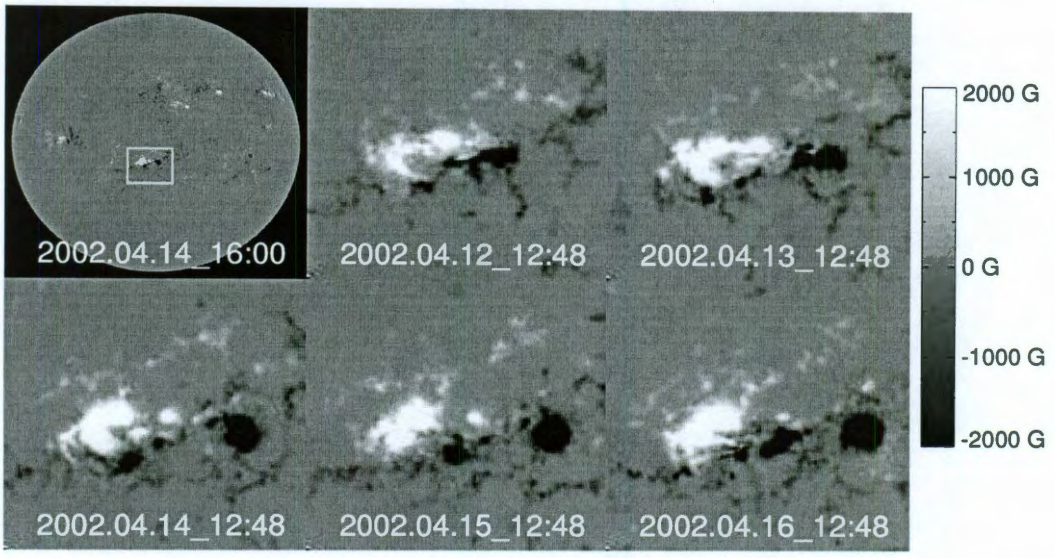

Figure 3.12 : MDI observations of AR 9906.

AR 9906 is an emerging active region first observed on the east limb on Apr. 11, 2002. It was located in the southern hemisphere, composed of a negative leading polarity and positive following polarity. The magnetic observations from SOHO/MDI are provided in Fig. 3.12. With the area of this active region increasing from Apr. 11 to Apr. 16, its magnetic type changes from β into complex $\beta\gamma\delta$ (see Table 3.2.3).

The maps of tangential velocity and magnetic helicity injection are shown in Fig. 3.13. At 12:48 UT, Apr. 15 2002, the magnetic helicity is injected mainly from three regions: the first two are the two polarities with clockwise rotation, while the third one is the newly emerged and fast moving negative polarity near the following polarity.

So, in this case, both the clockwise rotations and the braiding motion contributes to the positive helicity injection into the southern hemisphere corona.

Table 3.4 : Location and magnetic class of AR 9906.

Date	Position	Area	magnetic type
2002 Apr. 12	S16E40	80	β
2002 Apr. 13	S16E26	190	$\beta\gamma$
2002 Apr. 14	S15E13	470	$\beta\gamma\delta$
2002 Apr. 15	S15W02	640	$\beta\gamma\delta$
2002 Apr. 16	S15W14	690	$\beta\gamma$

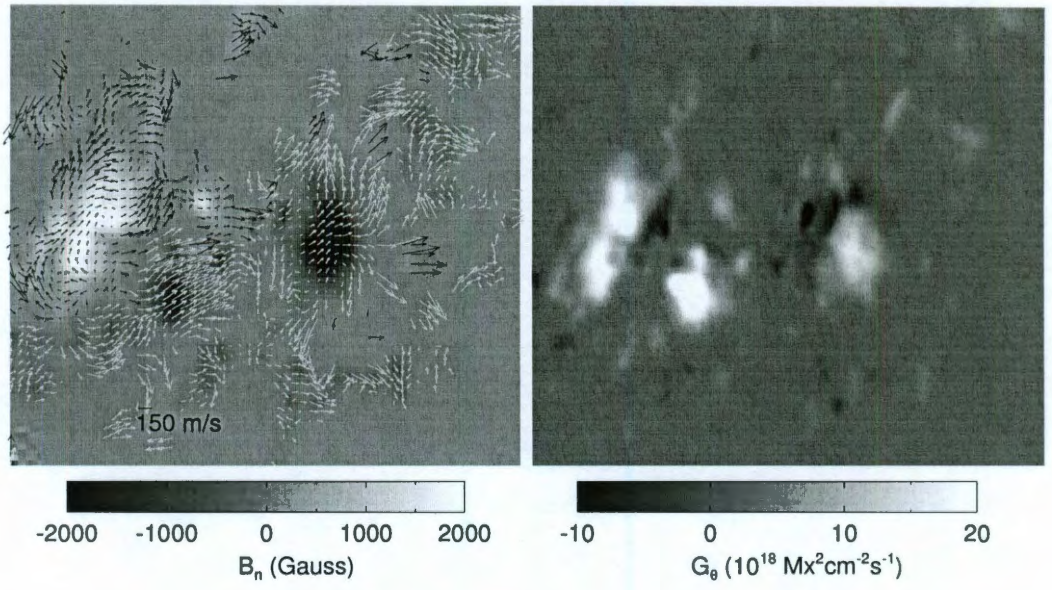

Figure 3.13 : left: Map of velocity superposed on the gray-scale map of B_n. Right: Gray-scale map of magnetic helicity flux density G_θ at 12:48, Apr.15.

The magnetic helicity injection is also imbalanced for AR 9906, with the amount from the rotating leading polarity significantly larger than that from the following one

(Fig. 3.14). For this event, both polarities contribute to the positive helicity injection. From Apr. 12 to 16, 2002, the total magnetic helicity injection is $9.2 \times 10^{43} Mx^2$.

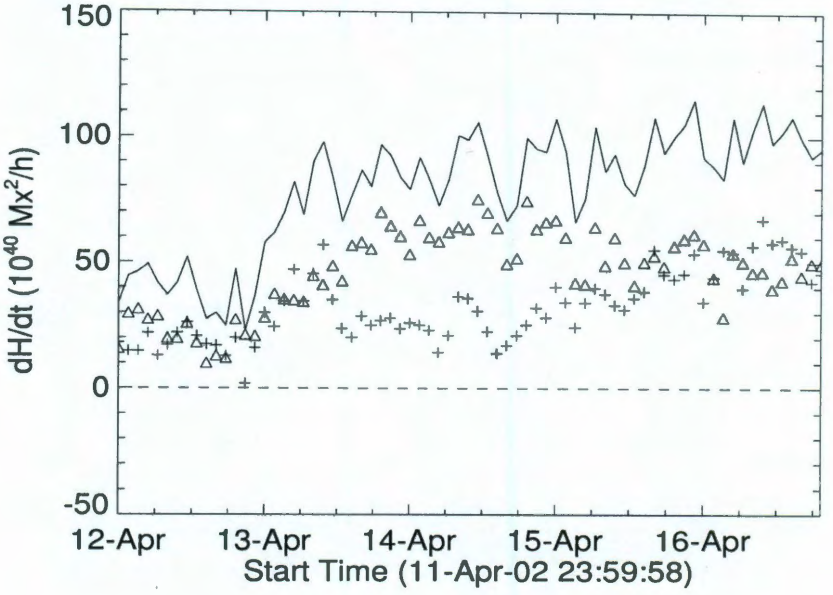

Figure 3.14 : Magnetic helcity injection rate of AR 9906 during Apr. 12 to 16.

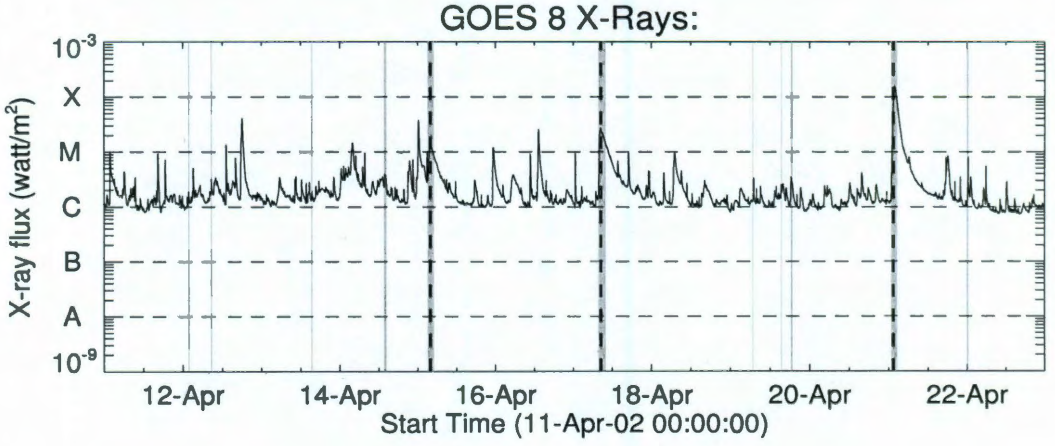

Figure 3.15 : Soft X-ray flux from Apr. 11 to Apr. 22, 2002.

Along with the accumulation of the magnetic helicity in the solar corona, AR 9906 began to display stronger solar activity. The observation of X-ray flux is shown in Fig. 3.15. The shaded regions denote the solar flares in AR 9906, while the vertical dashed lines show the time when SOHO/LASCO observed halo CMEs (see http://cdaw.gsfc.nasa.gov/CME_list/). These halo CMEs (see Table 3.5) erupted after Apr. 15, 2000, when there had already been a large amount of magnetic helicity injected in to AR 9906.

Table 3.5 : Halo CMEs and associated flares from AR 9906.

Date	F_{start}	F_{end}	position	F_{class}	T_{CME}	$v_{CME}(km/s)$
2002-04-15	03:05:00	05:06:00	S15W01	M1.2	03:50:05	720
2002-04-17	07:46:00	09:57:00	S14W34	M2.6	08:26:05	1240
2002-04-21	00:43:00	02:38:00	S14W84	X1.5	01:27:20	2393

3.2.4 AR 9165

On Sep. 15, 2000, AR 9165 appeared at about N12E30 as a β type, and evolved into $\beta\gamma$ in association with the growth of the area. This active region had a large tilt angle, almost perpendicular to the equator. After Sep. 16, this active region began to decay (see Fig. 3.16).

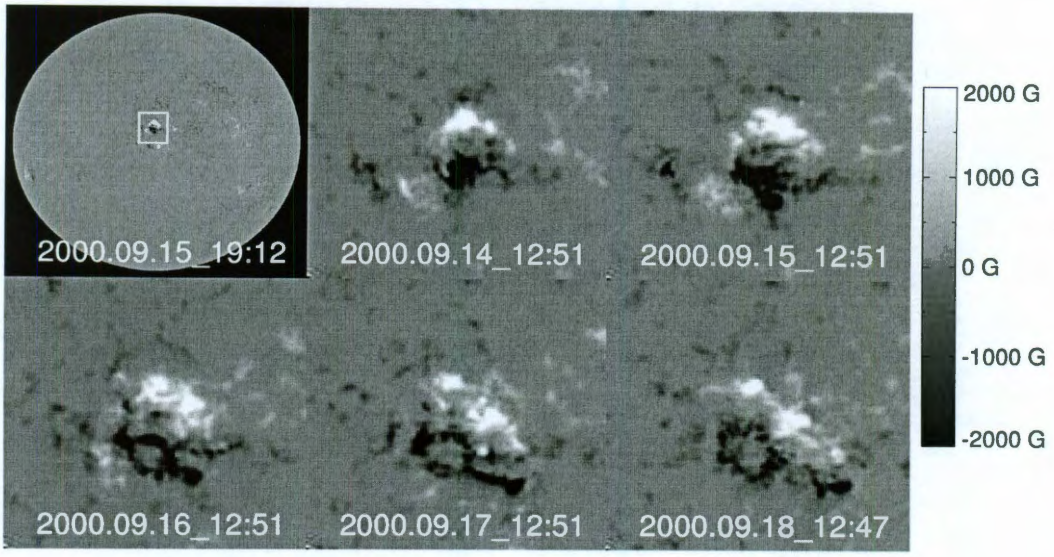

Figure 3.16 : SOHO/MDI observations of AR 9165.

The magnetic helicity injection from AR 9165 is primarily due to two regions, as shown in Fig. 3.17. The first source is the largest dark region in the map of helicity injection, which corresponds to a counter-clockwise rotation of the negative polarity. The second one is the comparably smaller dark region, due to the clockwise motion of the positive polarity around the negative one, i.e., the braiding motion. Both of the motions brought negative helicity from the convection zone into the northern hemisphere.

The helicity injection mainly occurred during the emerging period between Sep. 14 and Sep. 17, which is illustrated in Fig. 3.18. The peak value of the injection is a bit more than $-6 \times 10^{41} Mx^2/h$ during Sep. 15, with a large portion due to the rotation of the negative polarity. This results in the asymmetry of magnetic helicity injection for AR 9165.

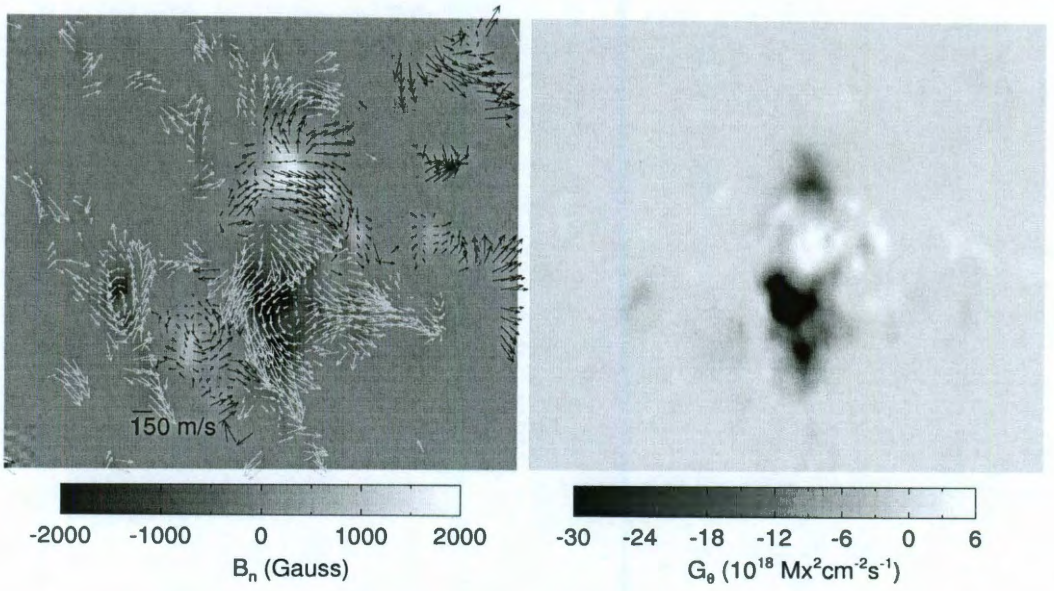

Figure 3.17 : left: Map of velocity superposed on the gray-scale map of B_n. Right: Gray-scale map of magnetic helicity flux density G_θ at 22:24, Sep. 14.

The total magnetic helicity injection is about $-2.4 \times 10^{43} Mx^2$. Fig. 3.19 gives the X-ray flux from the GOES satellite during the observations of AR 9165. Nindos et al. (2002) identified 5 CMEs associated with this active region. A M5.9 class flare was observed beginning at 04:07 UT, peaking at 04:17 UT on Sep. 16, 2000. Then a halo CME with a velocity of 1215 km/s was reported at 05:18 UT (Guo et al., 2007), denoted by a vertical dashed line in Fig. 3.19. This halo CME was also observed by WIND satellite at 1 AU near the Earth on Sep. 18. The average magnetic helicity of the magnetic clouds in 2000 is about $-7.7 \times 10^{42} Mx^2$ (Nindos et al., 2002). So the total magnetic helicity of these five CMEs is about $-3.8 \times 10^{43} Mx^2$, which is comparable to the magnitude of the total helicity injection from AR 9165, considering the possible underestimation of the helicity calculation with the magnetograms of 96 minutes (Tian et al., accepted) and the uncertainties of the total helicity of these five

CMEs. So the accumulation of negative helicity in AR 9165 might be a driver for the observed CMEs.

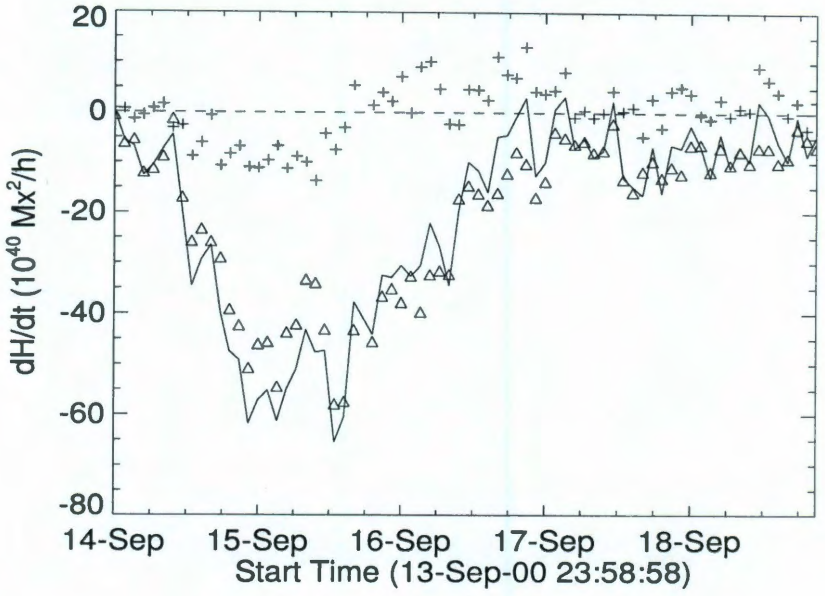

Figure 3.18 : Magnetic helcity injection rate of AR 9165 during Apr. 14 to 18, 2000.

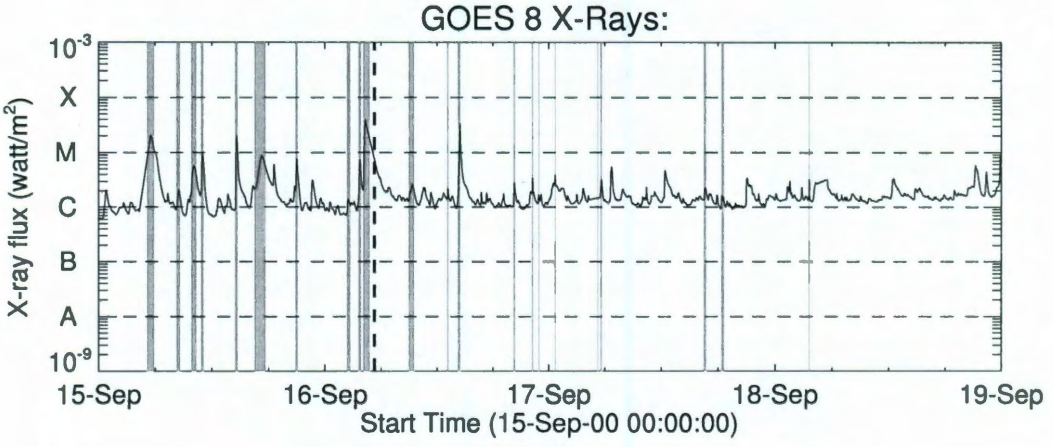

Figure 3.19 : Soft X-ray flux from Sep. 15 to Sep. 18, 2000.

Table 3.6 : Summary of the rotating sunspots in the four active regions.

active region	AR 9114	AR 10696	AR 9906	AR 9165
date	Aug. 6–10, 2000	Nov. 3–7, 2004	Apr. 12–16, 2002	Sep. 14–18, 2000
latitude	N12	N09	S16	N12
rotation	180°	90°	150°	50°
direction	↺	↺	↻	↺
max flare	C2.3	X2.0	M1.2	M5.9
$H_t(Mx^2)$	-3.4×10^{43}	-6.3×10^{43}	9.2×10^{43}	-2.4×10^{43}
	sigmoid	kinked filament	fast CMEs	fast CMEs
feature	CME	fast CMEs		mag. clouds
	mag. cloud			

The properties of the rotating sunspots in the four active regions are summarized in Table 3.6. Three active regions were located in the northern hemisphere and had negative total helicity injection, while one active region (AR 9906) in the southern hemisphere had positive total helicity injection. This result corresponds to the hemispheric helicity rule (e.g. Pevtsov, 2007). For the four active regions discussed, large helicity injections occurred during the period of rotation in polarities with strong magnetic field. This may be a result of the emergence of a twisted magnetic flux rope. For AR 9114 and AR 9165, magnetic clouds associated with these active regions are observed, and the helicity estimation (e.g. Nindos et al, 2003) shows that the total magnetic helicity injection in each active region and the helicity carried by the magnetic clouds are comparable.

3.3 Relation of helicity injection and solar flare index

Several studies have been done to study the magnetic helicity change and its relationship to solar flares. Moon et al. (2002) proposed that a sudden helicity injection may trigger flares. Kusano et al. (2003) suggested annihilation of magnetic

helicity as a triggering mechanism for flares. Here we give our preliminary study on the relation of the magnetic helicity injection and the flare productivity of the active regions.

To quantify the flare productivity of each active region, we adopt the daily soft X-ray flare index (Antalova, 1996), which is defined by weighting the flares of classes B, C, M, and X as 0.1, 1, 10, and 100, respectively. The flare index is written as

$$A = (100S^{(X)} + 10S^{(M)} + 1S^{(C)} + 0.1S^{(B)})/\tau$$

where $S^{(j)} = \sum_{i=1}^{N_j} I_i^{(j)}$ is the sum of the peak intensities of a certain class (i.e., sum of digits after the letters B, C, M, X) and τ is the total days of observation of the active region. Here the observation results by GOES satellites are used to calculate the flare index. In order to study the relation between the helicity injection and the daily flare index, the magnitude of daily total helicity injection (H_d) is adopted, i.e., $H_d = H_t/T$, where H_t is the total helicity injection during the period of T (unit: days).

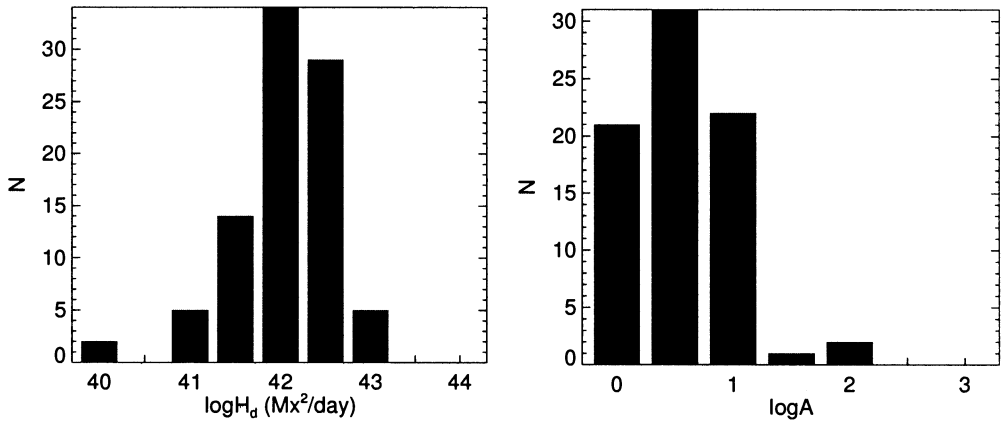

(a) (b)

Figure 3.20 : Distribution of the daily magnetic helicity injection H_d (a) and the flare index A (b) for 90 ARs, with the x-axis shown in the logarithm.

There are 90 active regions chosen for this study (the criterion of these ARs is introduced in chapter 4). The distributions of the daily helicity injection and the flare index are shown in Fig. 3.20. The average value of the daily helicity injection is about $3.2 \times 10^{42} Mx^2/day$, and the flare indexes mainly distribute between 0 and 30.

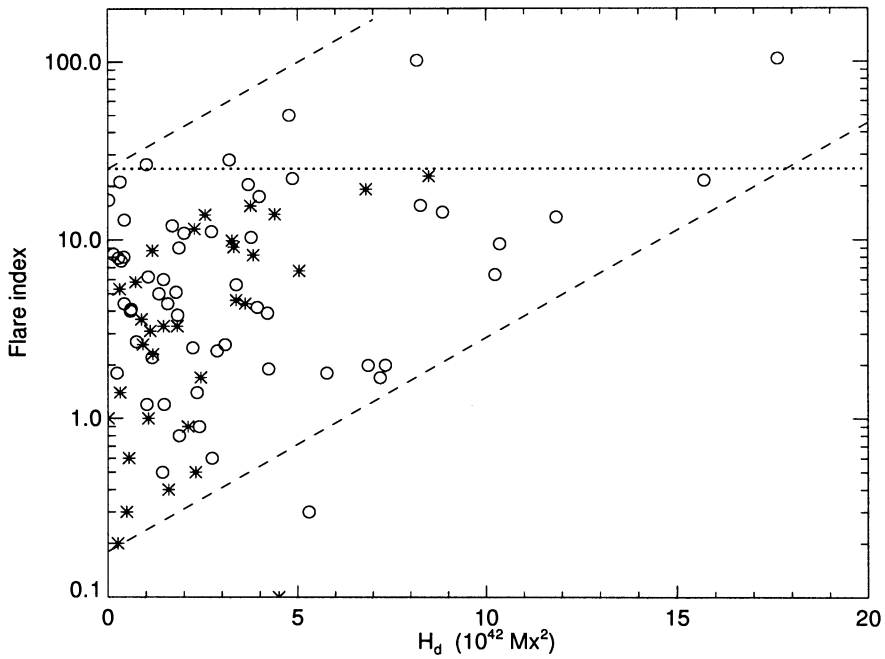

Figure 3.21 : Plot showing relation of magnetic helicity injection and solar flare index. $\circ$ ($\ast$) denotes the active region which contains sunspot with angular velocity greater (smaller) than $0.3^o/h$.

Fig. 3.21 shows the relation between the daily helicity injection and the flare index. In this figure, circles (asterisks) denote the faster (slower) sunspots with average rotating speed greater (less) than an arbitrary value of $0.3^o/h$. Generally, the slower sunspots have lower daily magnetic helicity injections ($5.0 \times 10^{42} Mx^2/day$) and show less flare productivity ($A < 25$, shown by horizontal dotted line). The daily helicity injection of the faster rotating sunspots covers a wide range, from 1.0×10^{41} to

$18.0 \times 10^{43} Mx^2/day$, while the flare index ranges from 0 to 105. For most active regions (except two), the relationship can be bounded by two boundaries, shown as dashed lines in Fig. 3.21. We see that as the daily helicity injection increases, the active regions tends to show higher flare activity. The width between the two boundaries may result from some delay (a few days) between the storage of free energy due to magnetic helicity injection and the solar productivity, so that while the helicity injection is observed to be large, the flare index may be still small. Further studies need to be done for better understanding of this phenomenon.

3.4 Discussion

In order to study the relation of rotating sunspots and magnetic helicity injection, four active regions (AR 9114, AR 10696, AR 9906, AR 9165) are investigated in this chapter. Among the four cases, three were located in the northern hemisphere and had negative total helicity injection, while one active region (AR 9906) located in the southern hemisphere had positive total helicity injection. So all these four active regions correspond to the hemispheric helicity rule (e.g. Pevtsov, 2007). The magnetic helicity injection can result from two motions: the rotation of sunspot and their braiding motion around another. For the four active regions discussed, large helicity injections occurred during the period of rotation in polarities with strong magnetic field. This may be a result of the emergence of a twisted magnetic flux rope. Moreover, the asymmetry of magnetic helicity injection (Tian and Alexander, 2009) between two polarities is confirmed here in the four cases, with the total helicity injection through one polarity usually three times larger than that through the other one.

For AR 9114 and AR 9165, magnetic clouds associated with these active regions

are observed by the WIND spacecraft near the Earth. The helicity estimation (e.g. Nindos et al, 2003) shows that the total magnetic helicity injection in each active region and the helicity carried by the magnetic clouds are comparable.

There are 90 active regions chosen for the preliminary study of magnetic helicity injection and the flare productivity for the active regions. The slower sunspots show lower daily magnetic helicity injections and have less flare productivity. While both the daily helicity injection and the flare index of the faster rotating sunspots covers a wide range.

Chapter 4

Observations of the velocity of rotating sunspots

4.1 Introduction

Sunspots are frequently observed to exhibit a prolonged period of rotation about their center (e.g., Brown et al., 2003). Several mechanisms have been introduced to explain this phenomenon. For example, Bao et al. (2002) summarized possible explanations, such as the observed differential rotation of the solar surface, the Coriolis force due to solar rotation, the $\alpha-$effect where structures are twisted as they rise through the solar convection zone to emerge as sunspots, and local surface flows. Simulations (Magara et al., 2001; Gibson et al., 2004; Fan, 2009) typically show that rotating sunspots are prevalent during the emergence of a twisted flux tube ($\Omega-$loop). Brown et al. (2003) pointed out that flux-tube emergence would be one important mechanism for rotating sunspots, but they also pointed out that further analysis was needed to determine the primary mechanism responsible for the rotating sunspots. Moreover, theoretical studies showed that the flux-tube would be expected to spin about its axis, resulting from a net axial torque, when the tube's twist varies along its axis (Longcope et al., 2000); Fan (2009) confirmed this study with a 3D simulation.

The relation between the emergence of the twisted flux tube and sunspot rotation still remains unclear, and the answer to this question would help us get a better understanding on the the solar dynamo and flux emergence processes occurring below the solar surface. In this chapter, we present a statistical study of the relation between

the rotation velocity of the sunspots and the emergence of the active regions. In addition, the phenomenon of multiple rotating sunspots in the same active region is shown and discussed.

4.2 Relation between rotating sunspots and emergence of active regions

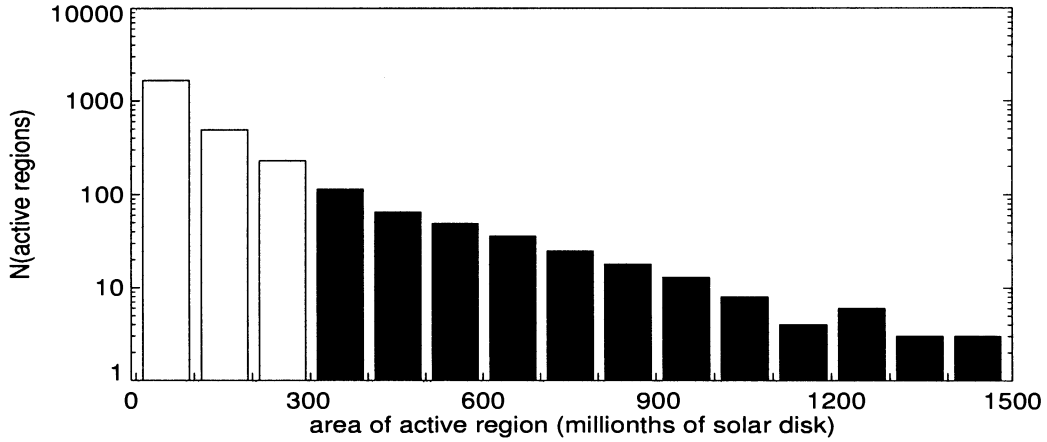

Figure 4.1 : Size distributions of the active regions from Dec., 1997 to Dec., 2005.

In this study, we apply the SOHO/MDI line-of-sight magnetograms, with temporal resolution of 96 minutes and spatial resolution of about 2″. There are 2727 active regions reported by NOAA (National Oceanic and Atmospheric Administration) between Dec. 1997 and Dec. 2005. The size distributions of these active regions are shown in Fig. 4.1 (ten active regions with size bigger than 1500 millionths of a solar disk are not included in this figure). The criteria for selection of the active regions are as following: 1) size of each active region is bigger than 300 millionths of solar disk (shown as dark in Fig. 4.1); 2) the active region is located near the center of the solar

disk, in the region surrounded by $\pm 50EW$ and $\pm 50NS$; 3) there is no evidence for magnetic saturation in the MDI data; 4) active region has a simple bipolar magnetic configuration. As a result, 132 sunspots in 95 active regions were selected for this study* .

Before we proceed to the calculation of the flow field with the DAVE method (see chapter 2), all images of an active region are cropped and derotated, so that the effect of solar differential rotation has been effectively excluded.

In order to determine whether each selected active region is emerging or not, the distance (denoted by "R_{pn}") between the flux-weighted centers of the leading and following polarities is calculated. One thing to mention is that, the active regions usually show morphological asymmetries (Fan 1993,; Tian & Alexander 2009), i.e., the leading sunspots tend to be coherent and compact, while the following sunspots tend to be dispersed and fragmented. As a result, the magnetic flux weighted center (e.g. Tian 2005) is determined as the centroid position of the particular magnetic polarity, using

$$x_c = \frac{\sum x(i,j)B_n(i,j)ds}{\sum B_n(i,j)ds} \qquad \& \qquad y_c = \frac{\sum y(i,j)B_n(i,j)ds}{\sum B_n(i,j)ds} \tag{4.1}$$

where B_n is the normal component of the magnetic field (based on the assumption that the strong magnetic field is normal to the solar surface, e.g., Solanki, 2003), $x(i,j)$ and $y(i,j)$ denotes the position of a pixel on the magnetogram with magnetic field strength of $B_n(i,j)$, and ds is the subregion that the selected sunspot or the polarity covers.

* Among these samples, there are 12 sunspots which show evolutions from the emergence to non-emergence phase as time goes on. Because of this, these sunspots appear in two different studies: the emergence study and the non-emergence study. But when they do we restrict considerations to the relevant phase.

We provide a quantitative description of specific examples of the kind of behaviours observed in this sample of rotating sunspots in the following subsections.

4.2.1 Rotation of sunspots during the emergence of active regions

AR 9563 was observed in the northern hemisphere from Aug. 2 to Aug 14, 2001, lying 20° from the equator. From Aug. 8 to Aug.11, it was near the center of the solar disk, and had a bipolar magnetic configuration, i.e., a β type sunspots group. During these 4 days, the leading sunspot in AR 9563 was observed to rotate clockwise, though a total angle of about 130°.

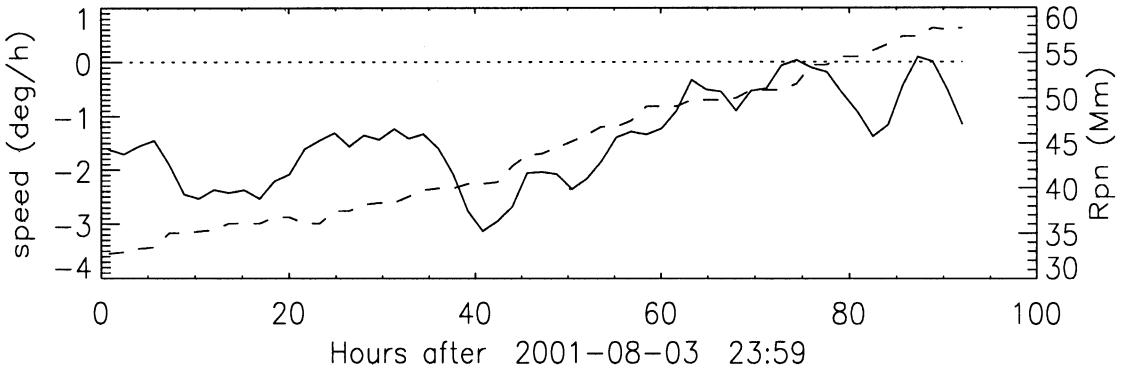

Figure 4.2 : Angular velocity profile (solid line) of the leading sunspot in AR 9563. The increasing footpoint separation (dashed line) indicates this is an emerging active region.

Fig. 4.2 shows the rotation speed of the leading sunspot of AR 9563, denoted by the solid line, while the separation distance between the two polarities is denoted by the dashed line (we use the same notation for the following figures). During the 4-day set of observations, the separation distance increases gradually from 34 Mm to 58 Mm, indicating that AR 9563 is emerging during this period. The average angular velocity of the leading sunspot is about $1.4°/h$, with a peak value of $3°/h$. Moreover,

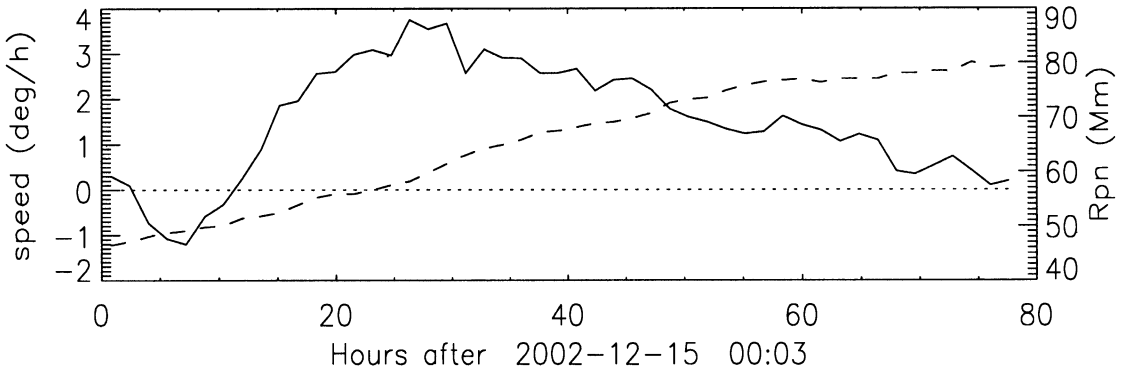

Figure 4.3 : Angular velocity profile (solid line) of the leading sunspot in AR 10226. The increasing footpoint separation (dashed line) indicates this is an emerging active region.

the direction of its rotation remains clockwise throughout the observational period. This, then, is an example of a rotating sunspot in an emerging this active region.

The leading sunspot in AR 10226 is another example of sunspot rotation occurring during the emergence of the active region. It was in the southern hemisphere, with a latitude of about $25°S$. During the period of 80 hours after Dec. 15, 2002, it predominantly rotated counter-clockwise, through a total angle of 102°. Fig. 4.3 shows the relation of the angular rotation speed to the emergence of AR 10226. The separation between the two polarities increases from 45 Mm to 80 Mm, indicating an emerging active region. Over the first ten hours, this sunspot shows slow clockwise rotation with a peak value of about $1°/h$. After that, it begins to show strong counter-clockwise rotation with a peak value of $3.7°/h$ during Dec. 16, 2002. Finally, the rotation speed gradually slows down until it stops rotating at the end of the observation.

However, not all the sunspots are found to show well-defined rotation during emergence. For example, a sunspot in the following polarity of AR 10036, which was

a $\beta\gamma\delta$ type active region, and shown in Fig. 4.4, exhibited a more complex rotation pattern. AR 10036 was located at the latitude of about $10°S$. During the 80 hours of observations from the start of July 20, 2002, its total rotation is less than 10°, with the average velocity of about $0.07°/h$, while the separation distance grew from 41 Mm to 50 Mm. Moreover, the direction of rotation is seen to change sign several times. In this study, we describe this kind of sunspot as a non-rotating during flux emergence (such complex rotation profiles require further and more sophisticated analysis).

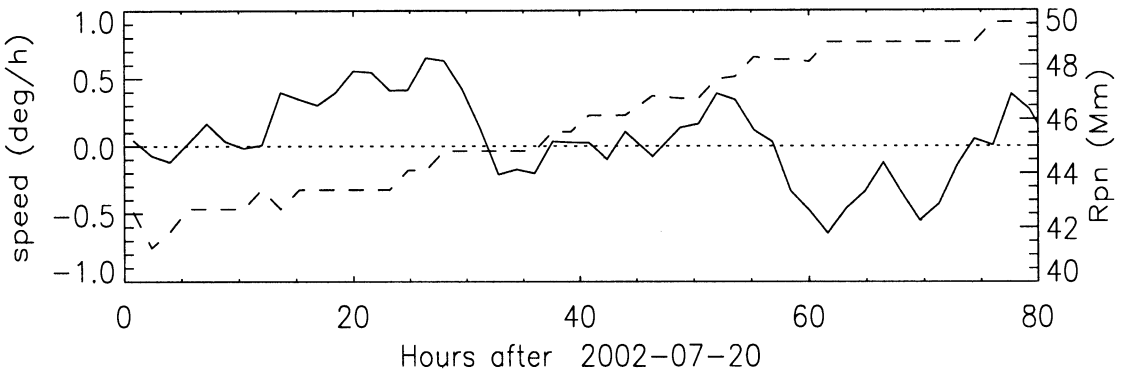

Figure 4.4 : Angular velocity profile (solid line) of the leading sunspot in AR 10036. The increasing footpoint separation (dashed line) indicates this is an emerging active region.

From our total sample, there are 82 sunspots identified to be associated with emerging active regions. Fig. 4.5(a) shows the rotation distribution of all 82 sunspots. The strongest rotation is detected for AR 9114, which had a total counter-clockwise rotation of about 180°. Among these sunspots, 76 are found be be rotating with average velocity greater than $0.2°/h$, as seen in Fig. 4.5(b), while the remaining 6 sunspots do not show well-defined rotation, exhibiting total rotations $\lesssim 10°$ and/or changes in rotating directions. Moreover, 59 sunspots exhibit rotations ranging from 20° to 100°. It is important to note that, as the observations usually do not cover the

whole emergence of the active regions, the real total rotations quoted are expected to be under-estimates.

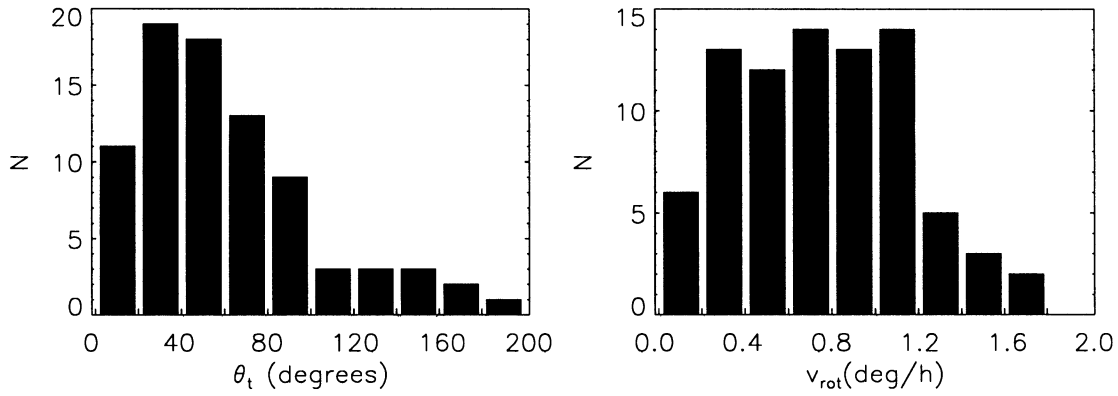

(a) (b)

Figure 4.5 : Total rotation (left) and angular velocity (right) distribution of 82 rotating sunspots associated with the emergence of an active regions.

In sum, among 82 active regions showing a growth of the separation of their two polarities, about 93% are associated with rotating sunspots, while the remaining 7% do not show well-defined or have complex rotational velocity profiles. This shows that rotating sunspots are strongly related to the emergence of flux tubes, confirming the expectations of Brown et al. (2003).

4.2.2 Rotations of sunspots after the emergence of the active regions

Among our selected sunspots, there are 50 sunspots that do not show a growth of their polarity separation. 30 of these sunspots are rotating, while the rest do not show well-defined rotation. Both examples are described in the following.

AR 9289 was located in the southern hemisphere with a latitude of $5°S$. From Dec. 31, 2000 to Jan. 3, 2001, its leading sunspot was seen to rotate about 50° clockwise.

The rotation profile is shown in Fig. 4.6. During this period, the separation distance is almost steady, staying at around 54 Mm. The leading spot mainly rotates clockwise, with an average speed of $0.56°/h$ and a peak value of about $1.5°/h$.

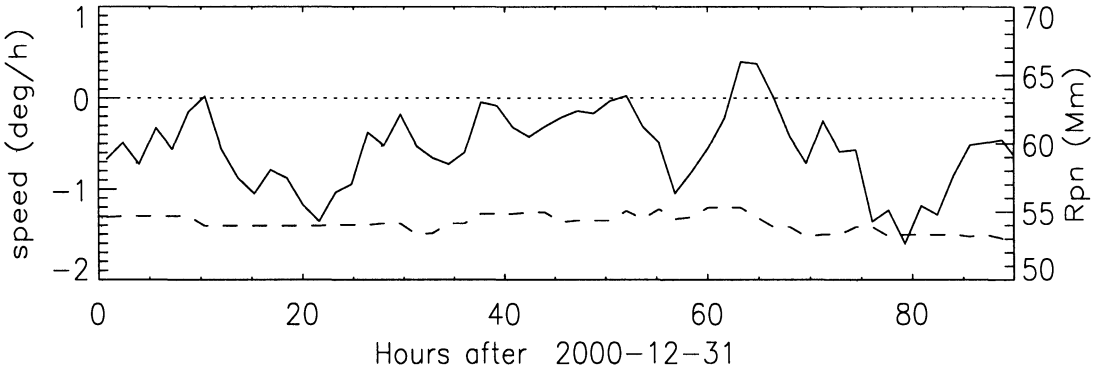

Figure 4.6 : Angular velocity profile of the leading sunspot in AR 9289.

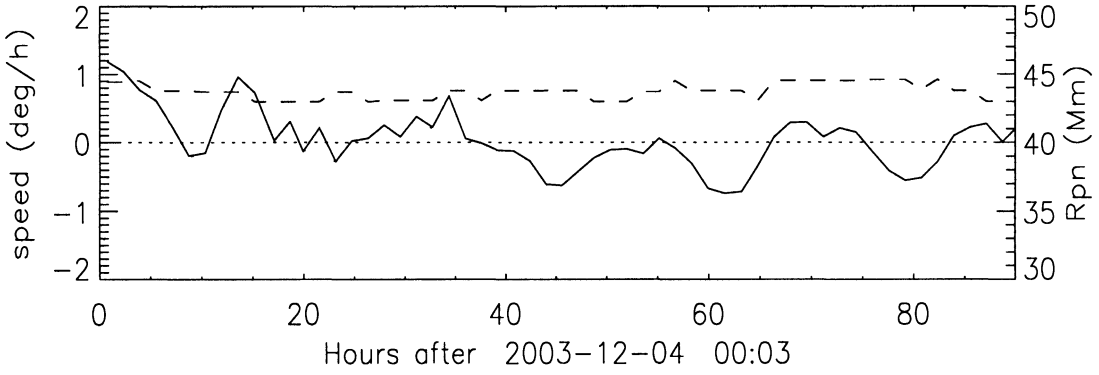

Figure 4.7 : Angular velocity profile of the leading sunspot in AR 10517 from Dec. 4, 2003 to Dec. 7, 2003.

Fig. 4.7 shows the velocity profile of the leading sunspot in AR 10517 from Dec. 4 to Dec. 7, 2003. This active region was in the southern hemisphere with a latitude of about $7°S$. It has a peak velocity of about $1°/h$, but it changes direction several times

during the course of the observation, leading to a very small total rotation angle of less than 10° and the average velocity of about $0.08°/h$.

Fig. 4.8 gives the distribution of total rotations (4.8(a)) and average angular velocities (4.8(b)) of all 50 sunspots that do not display a growth of separation distance between the leading and following polarities. 80% of these sunspots have total rotations less than 40° and 82% rotate with an average velocity of less than $0.5°/h$. Compared to Fig. 4.5, it is evident that, statistically, after the emergence of the active region has ceased, the sunspots tend to rotate slower than those that rotate during the emergence.

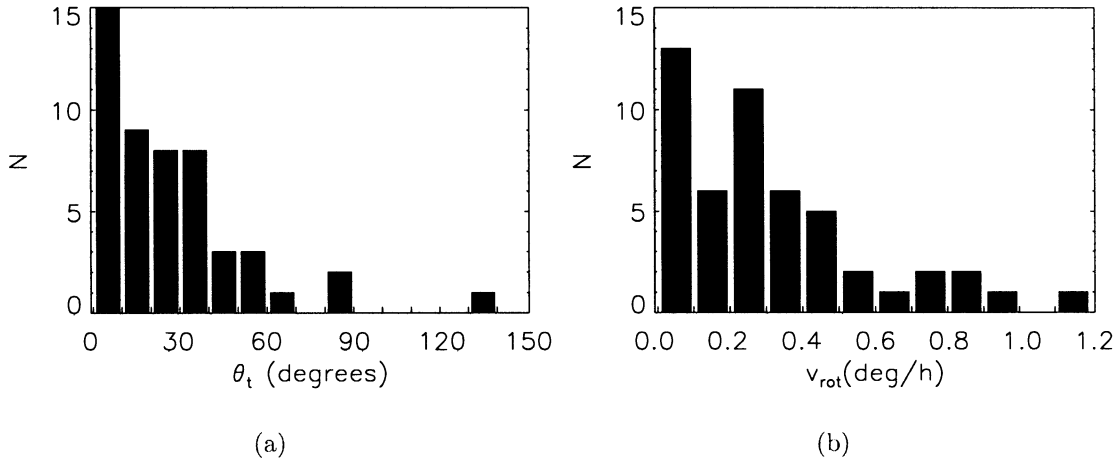

Figure 4.8 : Total rotation (left) and angular velocity distribution (right) of rotating sunspots after emergence.

In this section, we investigated 132 sunspots in 95 active regions to study the relationship between the rotating sunspots and the emergence of the active regions. Among 82 active regions which exhibit flux emergence, 93% are associated with rotating sunspots, showing a strong relation between the rotating sunspots and the

emergence of the flux tubes. Around 60% of 50 sunspots without well-defined emergence of the active regions, are observed to be still rotating, though relatively slowly.

4.3 Multiple rotating sunspots in the same active region

Occasionally, sunspots of both polarities in an active region are observed to be rotating; some rotate in the same direction (described as co-rotating sunspots here), others rotate in the opposite directions (counter-rotating sunspots). This section describes some observations of both types of multiple rotating sunspots in the same active region.

4.3.1 Co-rotating sunspots

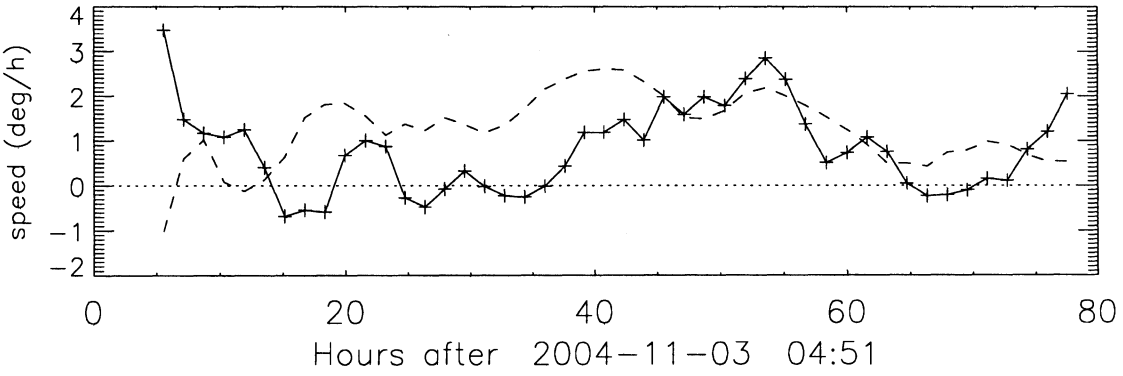

Figure 4.9 : Multiple rotating sunspots of both polarities in AR 10696.

The leading and following sunspots in AR 10696 rotated counter-clockwise during the period from Nov. 3 to Nov 6, 2004, as shown in Fig. 4.9. This active region was located in the Northern hemisphere with latitude of $9°N$. The peak values of the calculated rotation speed of both sunspots are about $3°/h$. The leading polarity

(denoted with dashed line) has an average velocity of $0.83°/h$ and a total rotation of about 80°, while the following polarity (solid line with '+') has an average velocity of $0.94°/h$ and total rotation of about 90°.

The scenario, in which sunspots in the active region rotate in the same direction, is believed to be more conducive for magnetic helicity injection and the subsequent storage of magnetic energy in the corona (e.g., Yan et al., 2008). For example, the co-rotating region discussed here, AR 10696, exhibited very strong coronal activity. Fig. 4.10 gives the X-ray flux between $0.1 - -0.8\ nm$ from Nov. 3 to Nov. 12, 2004, from the GOES satellite. There were 62 flares with magnitude greater than B6.8 reported during these days, shown as the shaded regions on Fig. 4.9. One X2.0 flare was reported by GOES and NOAA, from 15:42 to 16:15, Nov. 7; and another X2.5 flare began at 01:59 on Nov. 10, 2004.

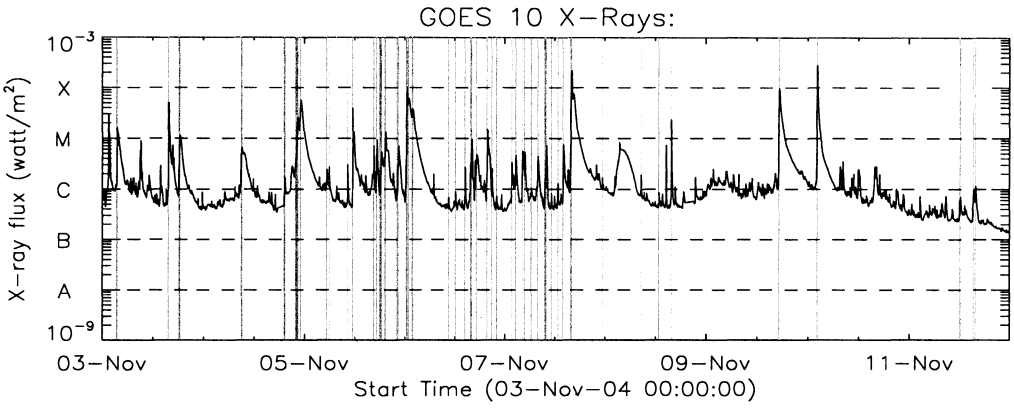

Figure 4.10 : GOES satellite observation of X-ray flux from Nov. 3 to Nov. 12, 2004. The shaded regions denote the flares in AR 10696.

Table 4.1 : Co-rotating sunspot groups. 'L': leading polarity, 'F': following polarity, θ_t: the total rotation, $\bar{v_\theta}$: average angular velocity, type: showing the active region is emerging or stable.

active region	θ_t	$\bar{v_\theta}$	type
8404(L)	34	0.56	emerging
8404(F)	60	1.05	emerging
8955(L)	-62	-0.53	stable
8955(F)	-29	-0.25	stable
9368(L)	42	0.34	emerging
9368(F)	89	0.75	emerging
9800(L)	29	0.3	emerging
9800(F)	27	0.24	emerging
9906(L)	-156	-1.68	emerging
9906(F)	-64	-0.71	emerging
10139(L)	-48	-1.2	emerging
10139(F)	-18	-0.43	emerging
10696(L)	78	0.83	emerging
10696(F)	88	0.94	emerging

In our sample of 95 active regions, there are 7 active regions found to contain co-rotating sunspots, as listed in Table 4.1. Six of these active regions are found to be emerging. The rotation of the two polarities can be quite different, such as in AR 10139, where the velocity of the leading polarity rotated about 3 times as fast as the following one.

4.3.2 Counter-rotating sunspots

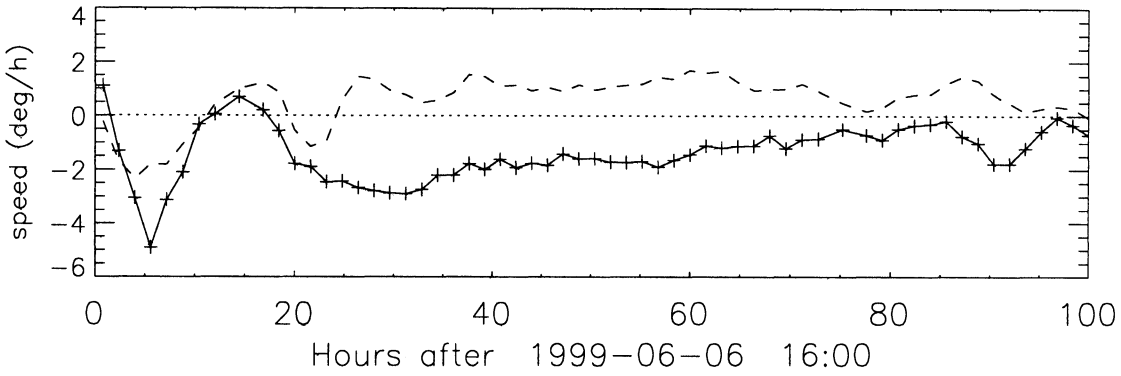

Figure 4.11 : Velocity profiles of sunspot rotation in AR 8574, an example of counter-rotating sunspot groups.

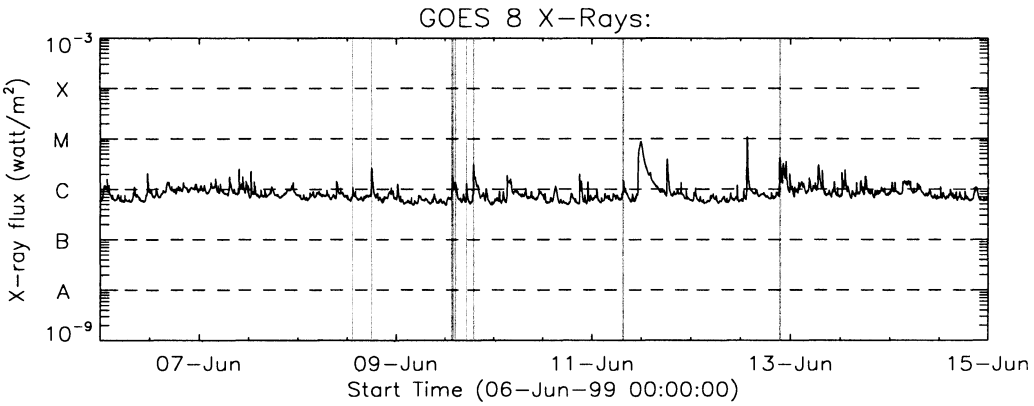

Figure 4.12 : GOES satellite observation of X-ray flux from Jun. 6 to Jun. 15, 1999. The shaded regions denote the flares in AR 8574.

Fig. 4.11 gives the rotation profile of the two polarities in AR 8574, an example of counter-rotating sunspots. From this figure, we can see that during the first 20 hours, the sunspots rotate in the same direction. After that, the rotation direction of the

following spot reverses. The leading polarity (solid line with '+') rotates about 180° clockwise, while the following one (dashed line) rotates about 90° counter-clockwise. A series of C class flares were reported in this active region, but no other stronger ones were produced, as shown in Fig. 4.12.

Table 4.2 lists 7 counter-rotating sunspot groups we found. Among these groups, 6 are in emerging active regions, while AR 9097 does not show significant polarity separation indicating that no, or minimal, flux emergence is taking place. AR 8574 showed the largest rotations, with the leading polarity rotating about 180°.

Table 4.2 : Counter-rotating sunspot groups. 'L': leading polarity, 'F': following polarity, θ_t: the total rotation, $\bar{v_\theta}$: average angular velocity, type: showing the active region is emerging or stable.

active region	θ_t	$\bar{v_\theta}$	type
8574(L)	-180	-1.17	emerging
8574(F)	94	0.68	emerging
8651(L)	-91	-0.96	emerging
8651(F)	24	0.26	emerging
9004(L)	40	0.95	emerging
9004(F)	-42	-0.97	emerging
9070(L)	79	1.04	emerging
9070(F)	31	0.41	emerging
9097(L)	-23	-0.2	stable
9097(F)	37	0.32	stable
10344(L)	97	1.05	emerging
10344(F)	-44	-0.5	emerging
10798(L)	-38	-0.87	emerging
10798(F)	35	0.74	emerging

In sum, 14 multiple rotating sunspot groups have been found in our study, including 7 co-rotating sunspot groups and 7 counter-rotating ones. Co-rotating sunspots are expected from the emergence of monolithic flux tubes, such as described by the

simulations of emerging uniformly twisted flux tubes done by Gibson et al. (2004). However, the counter-rotating sunspots pose a more difficult problem. One possibility relates to the theory of Loncope et al. (2000), which considers the case when the twists of the two polarities (footpoints of the assumed sunspot flux tube) are asymmetric. In this case, the twist would transfer from one polarity to the other one through the connecting loop in the corona (see also Fan, Alexander & Tian 2009), eventually leading to opposite signs of the twist gradient normal to the solar surface, causing counter-rotating sunspots (private communication, Fan, 2010).

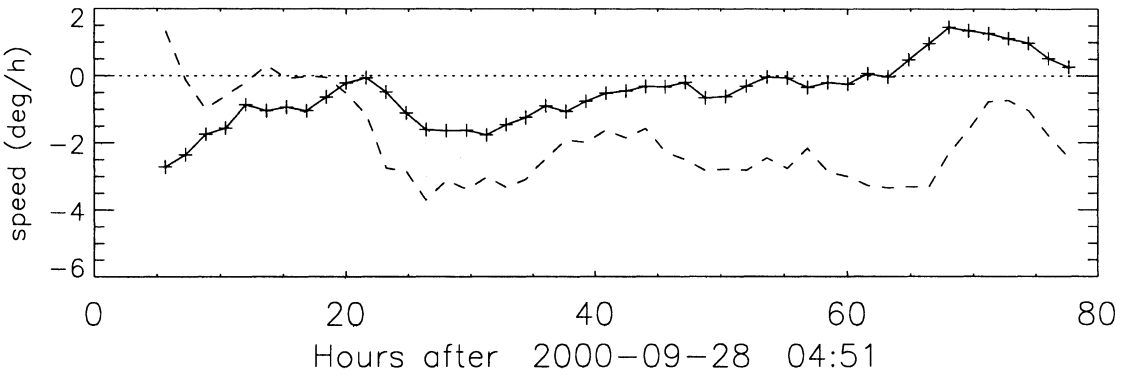

Figure 4.13 : Velocity profiles of sunspot rotation in AR 9173.

The rotating velocity profile of sunspots in AR 9173 could be an example of this scenario. The negative polarity (dashed line) continually rotates clockwise, while the positive polarity ('+' line) rotates clockwise in the first 60 hours, but changes into counter-clockwise rotation gradually in the following hours. However, how the asymmetrical twisted flux tube forms is still a mystery. Does it already exist under the convection zone prior to emergence, or is it formed through some processes happening in the convection zone? The answers to these questions are still not clear and need further consideration.

4.4 Hemispherical tendency of sunspot rotations

As the clockwise (counter-clockwise) rotation of sunspots implies positive (negative) magnetic helicity injection (e.g., Mandrini et al., 2004), and the hemispherical tendency expected from previous helicity studies (e.g. Pevtsov et al., 1995). So in this section, we study the hemispherical tendency of sunspot rotations.

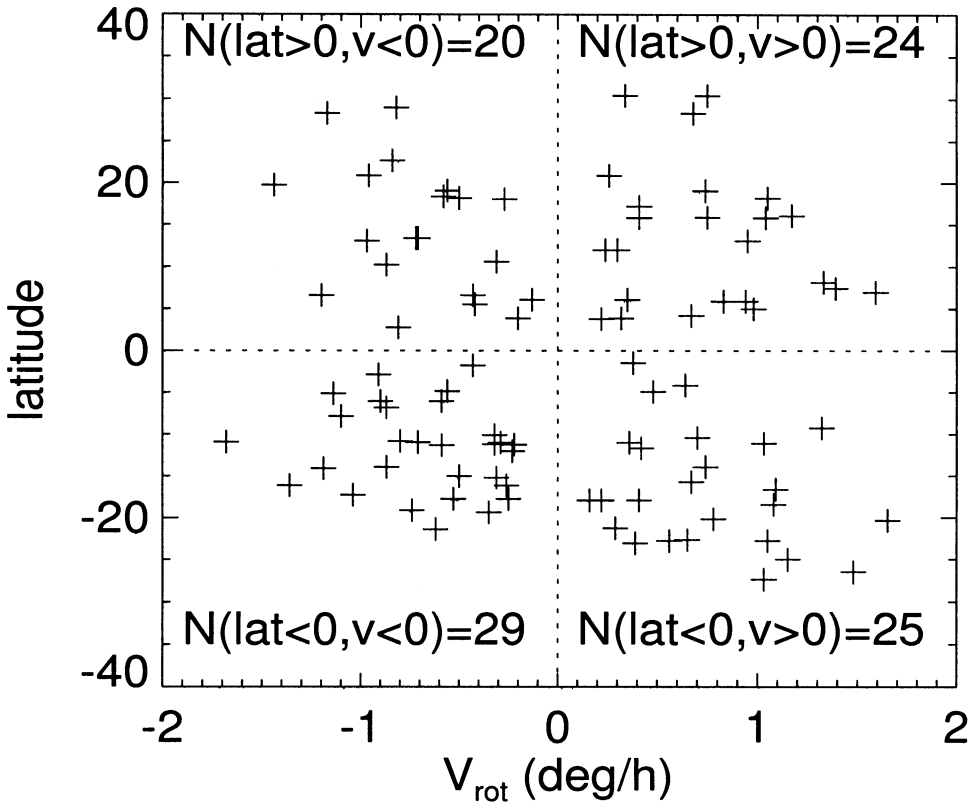

Figure 4.14 : Sunspot rotating tendency in both solar hemispheres. Negative velocity describes clockwise rotation, while positive velocity describes counter-clockwise rotation.

Fig. 4.14 shows the plot of latitude versus average velocity distribution of 98 rotating sunspots. In the northern hemisphere, there are 24 sunspots rotating counter-clockwise ($v_{rot} > 0$), and 20 sunspots rotating clockwise ($v_{rot} < 0$); In the southern

hemisphere, 25 sunspots rotate counter-clockwise, while 29 sunspots rotate clockwise. About 55% of the rotating sunspots in the northern hemisphere show counter-clockwise rotation, while 54% of the rotating sunspots in the southern hemisphere show clockwise rotation. So the rotations show a slight hemispherical tendency.

But the tendency here is weaker than the study of Pevtsov et al (1995), who measured the linear force-free field parameter α and showed that 76% of the active regions in the northern hemisphere have negative helicity, and 69% in the southern hemisphere have positive helicity. To better answer the hemispherical tendency observed for other solar phenomena, we would perform a study involving the braiding motions of sunspots, which could also contribute the magnetic helicity injection.

4.5 Discussion

In order to find the relation between rotating sunspots and the emergence of the active regions, 132 sunspots in 95 active regions were investigated. Among 82 active regions which exhibit flux emergence, 93% are associated with rotating sunspots, showing a strong relation between the rotating sunspots and the emergence of the flux tubes. Around 60% of 50 sunspots without well-defined active region emergence are observed to be still rotating, though relatively slowly. The rotating sunspots could be result from the projected velocity of emerging twisted flux tube (e.g., Démoulin et al., 2007) or from the existence of a twist gradient normal to the solar surface (Longcope et al., 2000). Both mechanisms would imply a strong relation between rotating sunspots and the emergence of active regions, as found in the analysis presented in this thesis. For the active regions without well-defined emergence, the projected velocity, if present, would be small, so the presence of rotating sunspots after the end of the emergence suggests that the balance of the twist near the photosphere has not yet

been reached, or is interrupted as a result of some processes, like solar flares (private communication, Fan, 2010).

There are 20 sunspot groups with both polarities investigated from the selected cases. Seven cases show co-rotating rotations, and another seven show counter-rotation. The co-rotation of two sunspots has a simple explanation related to the emergence of a twisted flux tube. However, the reason for the counter-rotating sunspots still need further consideration. Furthermore, among these 20 cases, 14 leading polarities have faster rotation than their following ones, indicating that the leading polarities tend to rotate faster than the following polarity (Tian and Alexander 2009). This result corresponds to the simulation result of Fan et al. (2009), which demonstrated that the leading leg of the flux tube had a higher rise velocity, resulting to a higher rotating velocity observed in this polarity.

To study the hemispherical tendency of sunspot rotations, 98 rotating sunspots are investigated. About 55% of the rotating sunspots in the northern hemisphere show counter-clockwise rotation, while 54% of the rotating sunspots in the southern hemisphere show clockwise rotation. This corresponds to a weak hemispherical tendency.

Chapter 5

Concluding remarks and future work

This thesis focuses on the magnetic helicity injection due to the rotating sunspots and the characteristics of the rotating sunspots in the active regions with simpler magnetic configurations. This chapter summarizes the main results of present work for this thesis and discusses future studies.

5.1 Datasets and the flow velocity inversion techniques

The magnetograms used in this thesis are mainly from SOHO/MDI, which was launched on Dec., 1995. The spatial resolution of the data applied here is about 2 arc-seconds and the temporal resolution is about 96 minutes. The magnetograms allows us to calculate the flow field on the solar surface with a few flow velocity inversion techniques, like LCT, DAVE, MEF, and DAVE4VM. Based on the comparisons of these methods and their availability for the line-of-sight magnetograms, the DAVE method has been chosen for our study on the rotating sunspots.

As the successor of SOHO/MDI, SDO/HMI (SDO: solar dynamic observatory; HMI: Helioseismic and Magnetic Imager) was launched on Feb. 11, 2010. The DAVE4VM method, which is thought to be able to recover 95% of the magnetic helicity rate (Schuck, 2008), would be coupled with the high resolution of the SDO/HMI data ($1''$ and 90 seconds*) to provide higher sensitivity and more accurate calculations

* http://jsoc.stanford.edu/doxygen_html

of the helicity injection in active regions.

5.2 Magnetic helicity injection and rotating sunspots

In chapter 3, four active regions (AR 9114, AR 9165, AR 9906, AR 10696) are investigated to study the relation of rotating sunspots and magnetic helicity. For these four cases, more helicity was injected during the period of rotation in polarities with strong magnetic field, which may result from the emergence of the flux rope. Together with the result of the helicity carried by the magnetic clouds (e.g. Nindos et al, 2003), it suggests that the active regions have comparable helicity budget for the magnetic clouds. Moreover, our preliminary study on 90 active regions shows that both the daily helicity injection and the flare index cover a wide range; and the upper and lower bounds of the flare index increase with the daily helicity injection.

Solar flares are thought to be able to redistribute the magnetic helicity in the solar corona, while CMEs are thought to take the magnetic helicity away from the sun (e.g. Démoulin et al., 2007). So, as the onset of flares or CMEs, the balance of twist at the interface between the interior and the corona could be broken, so that the rotation rate of the sunspots are supposed to be change (private communication, Fan, 2010). This would be investigated in the future work.

5.3 Characteristics of rotating sunspots

Chapter 4 gives a statistical study on the relation between rotating sunspots and the emergence of the flux tubes (in our study, the emergence is determined by the growth of the distance between two polarities in one active region), 132 sunspots in 95 active regions were investigated. Among 82 active regions which exhibit flux emergence, about 93% are rotating sunspots; while around 60% of 50 sunspots without

well-defined flux emergence are observed to be still rotating, though relatively slowly. Our result shows that two mechanisms, the projected velocity of emerging twisted flux tube (e.g., Démoulin et al., 2007) and existence of twist gradient normal to the solar surface (Longcope et al., 2000), can contribute to the observed rotation of the sunspots. Both mechanisms could play important roles for the rotating sunspots in emerging active regions, so that a strong relation would be expected. For the active regions without well-defined emergence, the observed rotation of sunspots suggests that the balance of the twist near the photosphere has not been reached, or has been interrupted as a result of some processes, like solar flares (private communication, Fan, 2010).

Moreover, about 55% of the rotating sunspots in the northern hemisphere show counter-clockwise rotation, while 54% of the rotating sunspots in the southern hemisphere show clockwise rotation. This corresponds to a weak hemispherical tendency.

Bibliography

[1] VI Abramenko. Relationship between magnetic power spectrum and flare productivity in solar active regions. *The Astrophysical Journal*, 629:1141, 2005.

[2] D. Alexander. An introduction to the pre-cme corona. *Space Science Reviews*, 123(1-3):81–92, 2006.

[3] D. Alexander. *The Sun*. Greenwood Press, 2009.

[4] A. Antalová. Daily soft x-ray flare index (1969–1972). *Contributions of the Astronomical Observatory Skalnate Pleso*, 26:98–120, 1996.

[5] SD Bao, T. Sakurai, and Y. Suematsu. The sources of magnetic field twist in solar active regions. *The Astrophysical Journal*, 573:445, 2002.

[6] M.A. Berger and G.B. Field. The topological properties of magnetic helicity. *Journal of Fluid Mechanics*, 147:133–148, 1984.

[7] A. Brandenburg and K. Subramanian. *Astrophysical magnetic fields and nonlinear dynamo theory*, volume 417. Elsevier, 2005.

[8] D.S. Brown, RW Nightingale, D. Alexander, CJ Schrijver, TR Metcalf, RA Shine, AM Title, and CJ Wolfson. Observations of rotating sunspots from trace. *Solar Physics*, 216(1):79–108, 2003.

[9] R.C. Canfield, H.S. Hudson, and D.E. McKenzie. Sigmoidal morphology and eruptive solar activity. *Geophysical Research Letters*, 26(6):627–630, 1999.

[10] J. Chae. Observational determination of the rate of magnetic helicity transport through the solar surface via the horizontal motion of field line footpoints. *The Astrophysical Journal Letters*, 560:L95, 2001.

[11] J. Chae. Measurements of magnetic helicity injected through the solar photosphere. *Advances in Space Research*, 39(11):1700–1705, 2007.

[12] R. Chandra, B. Schmieder, G. Aulanier, and JM Malherbe. Evidence of magnetic helicity in emerging flux and associated flare. *Solar Physics*, 258(1):53–67, 2009.

[13] S. Dasso, C. H. Mandrini, P. Demoulin, and C. J. Farrugia. Magnetic helicity analysis of an interplanetary twisted flux tube. *Journal of Geophysical Research-Space Physics*, 108(A10), 2003.

[14] P. Démoulin. Recent theoretical and observational developments in magnetic helicity studies. *Advances in Space Research*, 39(11):1674–1693, 2007.

[15] P. Démoulin. A review of the quantitative links between cmes and magnetic clouds. *Ann. Geophys*, 26:3113–3125, 2008.

[16] P. Demoulin, C. H. Mandrini, L. van Driel-Gesztelyi, B. J. Thompson, S. Plunkett, Z. Kovari, G. Aulanier, and A. Young. What is the source of the magnetic helicity shed by cmes? the long-term helicity budget of ar 7978. *Astronomy & Astrophysics*, 382(2):650–665, 2002.

[17] YJ Ding, QF Hong, and HZ Wang. A statistical study of the spiral spots on the solar disc. *Solar Physics*, 107(2):221–231, 1987.

[18] V. Domingo, B. Fleck, and AI Poland. The soho mission: an overview. *Solar Physics*, 162(1):1–37, 1995.

[19] J. Evershed. Radial movement in sun-spots (second paper). 1910.

[20] Y. Fan. The three-dimensional evolution of buoyant magnetic flux tubes in a model solar convective envelope. *Astrophysical Journal*, 676(1):680–697, 2008.

[21] Y. Fan. The emergence of a twisted flux tube into the solar atmosphere: Sunspot rotations and the formation of a coronal flux rope. *The Astrophysical Journal*, 697:1529, 2009.

[22] Y. Fan, D. Alexander, and L. Tian. On the origin of the asymmetric helicity injection in emerging active regions. *Astrophysical Journal*, 707(1):604–611, 2009.

[23] Y. Fan, G. H. Fisher, and E. E. Deluca. The origin of morphological asymmetries in bipolar active regions. *Astrophysical Journal*, 405(1):390–401, 1993.

[24] Y. Fan and S. E. Gibson. Numerical simulations of three-dimensional coronal magnetic fields resulting from the emergence of twisted magnetic flux tubes. *Astrophysical Journal*, 609(2):1123–1133, 2004.

[25] J. Finn and TM Antonsen. Comments on plasma phys. and contr. 26:111, 1985.

[26] T. G. Forbes. A review on the genesis of coronal mass ejections. *Journal of Geophysical Research-Space Physics*, 105(A10):23153–23165, 2000.

[27] S. E. Gibson, Y. Fan, C. Mandrini, G. Fisher, and P. Demoulin. Observational consequences of a magnetic flux rope emerging into the corona. *Astrophysical Journal*, 617(1):600–613, 2004.

[28] SE Gibson, Y. Fan, C. Mandrini, G. Fisher, and P. Demoulin. Observational consequences of a magnetic flux rope emerging into the corona. *The Astrophysical Journal*, 617:600, 2004.

[29] J. Guo, HQ Zhang, and OV Chumak. Magnetic properties of flare-cme productive active regions and cme speed. *Astronomy and Astrophysics*, 462(3):1121–1126, 2007.

[30] G.E. Hale. The fields of force in the atmosphere of the sun. *Nature*, 119(3002):708–714, 1927.

[31] G.E. Hale, F. Ellerman, S.B. Nicholson, and A.H. Joy. The magnetic polarity of sun-spots. *The Astrophysical Journal*, 49:153, 1919.

[32] BN Handy, LW Acton, CC Kankelborg, CJ Wolfson, DJ Akin, ME Bruner, R. Caravalho, RC Catura, R. Chevalier, DW Duncan, et al. The transition region and coronal explorer. *Solar Physics*, 187(2):229–260, 1999.

[33] AW Hood and ER Priest. Kink instability of solar coronal loops as the cause of solar flares. *Solar Physics*, 64(2):303–321, 1979.

[34] RF Howard, JW Harvey, and S. Forgach. Solar surface velocity fields determined from small magnetic features. *Solar Physics*, 130(1):295–311, 1990.

[35] K. Kusano, T. Maeshiro, T. Yokoyama, and T. Sakurai. Measurement of magnetic helicity flux into the solar corona. *Advances in Space Research*, 32(10):1917–1922, 2003.

[36] K. Kusano, T. Yokoyama, T. Maeshiro, and T. Sakurai. Annihilation of magnetic helicity: A new model for solar flare onset. *Advances in Space Research*, 32(10):1931–1936, 2003.

[37] R.J. Leamon, R.C. Canfield, S.L. Jones, K. Lambkin, B.J. Lundberg, and A.A. Pevtsov. Helicity of magnetic clouds and their associated active regions. *Journal of Geophysical Research*, 109(A5):A05106, 2004. http://www.agu.org/journals/ja/ja0405/2003JA010324/.

[38] J.A. Leese, C.S. Novak, and V. Ray Taylor. The determination of cloud pattern motions from geosynchronous satellite image data. *Pattern Recognition*, 2(4):279–280, 1970.

[39] RP Lepping, MH Acũna, LF Burlaga, WM Farrell, JA Slavin, KH Schatten, F. Mariani, NF Ness, FM Neubauer, YC Whang, et al. The wind magnetic field investigation. *Space Science Reviews*, 71(1):207–229, 1995.

[40] D. W. Longcope. Inferring a photospheric velocity field from a sequence of vector magnetograms: The minimum energy fit. *Astrophysical Journal*, 612(2):1181–1192, 2004.

[41] D. W. Longcope, G. H. Fisher, and A. A. Pevtsov. Flux-tube twist resulting from helical turbulence: The sigma-effect. *Astrophysical Journal*, 507(1):417–432, 1998.

[42] DW Longcope and BT Welsch. A model for the emergence of a twisted magnetic flux tube. *The Astrophysical Journal*, 545:1089, 2000.

[43] T. Magara and D. W. Longcope. Injection of magnetic energy and magnetic helicity into the solar atmosphere by an emerging magnetic flux tube. *Astrophysical Journal*, 586(1):630–649, 2003.

[44] W. Manchester IV, T. Gombosi, D. DeZeeuw, and Y. Fan. Eruption of a buoyantly emerging magnetic flux rope. *The Astrophysical Journal*, 610:588, 2004.

[45] CH Mandrini, P. Démoulin, L. van Driel-Gesztelyi, L. Van Driel-Gesztelyi, L. Van Driel-Gesztelyi, L.L.M. Van Driel-Gesztelyi, and M.C.L. Fuentes. Magnetic helicity budget of solar-active regions from the photosphere to magnetic clouds. *Astrophysics and Space Science*, 290(3):319–344, 2004.

[46] EW Maunder. The sun and sun-spots, 1820-1920. *Monthly Notices of the Royal Astronomical Society*, 82:534–543, 1922.

[47] Y.J. Moon, J. Chae, GS Choe, H. Wang, YD Park, HS Yun, V. Yurchyshyn, and P.R. Goode. Flare activity and magnetic helicity injection by photospheric horizontal motions. *The Astrophysical Journal*, 574:1066, 2002.

[48] JJ Moreau. Constants dun ilot tourbillonnaire en fluide parfait barotrope. *CR Acad. Sci. Paris*, 252:2810–2812, 1961.

[49] D. Nandy, D.H. Mackay, R.C. Canfield, and PCH Martens. Twisted solar active region magnetic fields as drivers of space weather: Observational and theoretical investigations. *Journal of Atmospheric and Solar-Terrestrial Physics*, 70(2-4):605–613, 2008.

[50] A. Nindos and MD Andrews. The association of big flares and coronal mass ejections: What is the role of magnetic helicity? *The Astrophysical Journal Letters*, 616:L175, 2004.

[51] A. Nindos and H. Zhang. Photospheric motions and coronal mass ejection productivity. *The Astrophysical Journal Letters*, 573:L133, 2002.

[52] A. Nindos, J. Zhang, and H. Zhang. The magnetic helicity budget of solar active regions and coronal mass ejections. *The Astrophysical Journal*, 594:1033, 2003. AR 8210, 9114.

[53] L.J. November and G.W. Simon. Precise proper-motion measurement of solar granulation. *The Astrophysical Journal*, 333:427–442, 1988.

[54] E. Pariat, P. Demoulin, and A. Nindos. How to improve the maps of magnetic helicity injection in active regions? *Advances in Space Research*, 39(11):1706–1714, 2007.

[55] E. Pariat, A. Nindos, P. Démoulin, and MA Berger. What is the spatial distribution of magnetic helicity injected in a solar active region? *Astronomy and Astrophysics*, 452(2):623–630, 2006. AR 9114.

[56] S.H. Park, J. Chae, and H. Wang. Productivity of solar flares and magnetic helicity injection in active regions. *The Astrophysical Journal*, 718:43, 2010. AR 10696.

[57] E.N. Parker. Hydromagnetic dynamo models. *The Astrophysical Journal*, 122:293, 1955.

[58] A. A. Pevtsov, R. C. Canfield, and T. R. Metcalf. Latitudinal variation of helicity of photospheric magnetic-fields. *Astrophysical Journal*, 440(2):L109–L112, 1995.

[59] A.A. Pevtsov. What helicity can tell us about solar magnetic fields. *Journal of Astrophysics and Astronomy*, 29(1):49–56, 2008.

[60] B. Ravindra, D. W. Longcope, and W. P. Abbett. Inferring photospheric velocity fields using a combination of minimum energy fit, local correlation tracking, and doppler velocity. *Astrophysical Journal*, 677(1):751–768, 2008.

[61] P. W. Schuck. Tracking magnetic footpoints with the magnetic induction equation. *Astrophysical Journal*, 646(2):1358–1391, 2006.

[62] P. W. Schuck. Tracking vector magnetograms with the magnetic induction equation. *Astrophysical Journal*, 683(2):1134–1152, 2008.

[63] M. Sobotka, P.N. Brandt, and G.W. Simon. Fine structure in sunspots. i. sizes and lifetimes of umbral dots. *Astronomy and astrophysics*, 328:682–688, 1997.

[64] S.K. Solanki. Sunspots: an overview. *Astronomy and Astrophysics Review*, 11(2):153–286, 2003.

[65] M. Stix. *The sun: an introduction*. Springer Verlag, 2004.

[66] P. Subramanian and KP Dere. Source regions of coronal mass ejections. *The Astrophysical Journal*, 561(1):372–395, 2001.

[67] L. R. Tian and D. Alexander. Role of sunspot and sunspot-group rotation in driving sigmoidal active region eruptions. *Solar Physics*, 233(1):29–43, 2006.

[68] L. R. Tian and D. Alexander. Asymmetry of helicity injection flux in emerging active regions. *The Astrophysical Journal*, 695:1012, 2009.

[69] L. R. Tian, D. Alexander, Y. Liu, and J. Yang. Magnetic twist and writhe of delta active regions. *Solar Physics*, 229(1):63–77, 2005.

[70] L. R. Tian, D. Alexander, and R. Nightingale. Origins of coronal energy and helicity in noaa 10030. *Astrophysical Journal*, 684(1):747–756, 2008.

[71] L. R. Tian, P. Demoulin, D. Alexander, and C. Zhu. On asymmetry of magnetic helicity in emerging active regions: High resolution observations. *Astrophysical Journal*, accepted.

[72] L. R. Tian, Y. Liu, J. Yang, and D. Alexander. The role of the kink instability of a long-lived active region ar 9604. *Solar Physics*, 229(2):237–253, 2005.

[73] Y. Wang and J. Zhang. A statistical study of solar active regions that produce extremely fast coronal mass ejections. *The Astrophysical Journal*, 680:1516, 2008.

[74] DF Webb and AJ Hundhausen. Activity associated with the solar origin of coronal mass ejections. *Solar Physics*, 108(2):383–401, 1987.

[75] B. T. Welsch, W. P. Abbett, M. L. DeRosa, G. H. Fisher, M. K. Georgoulis, K. Kusano, D. W. Longcope, B. Ravindra, and P. W. Schuck. Tests and comparisons of velocity-inversion techniques. *Astrophysical Journal*, 670:1434–1452, 2007.

[76] D. R. Williams, T. Torok, P. Demoulin, L. van Driel-Gesztelyi, and B. Kliem. Eruption of a kink-unstable filament in noaa active region 10696. *Astrophysical Journal*, 628(2):L163–L166, 2005.

[77] X.L. Yan, Z.Q. Qu, and D.F. Kong. Relationship between rotating sunspots and flare productivity. *Monthly Notices of the Royal Astronomical Society*, 391(4):1887–1892, 2008.

[78] XL Yan, ZQ Qu, and CL Xu. A statistical study on rotating sunspots: Polarities, rotation directions, and helicities. *The Astrophysical Journal Letters*, 682:L65, 2008.

[79] Y. Zhang, J. Liu, and H. Zhang. Relationship between rotating sunspots and flares. *Solar Physics*, 247(1):39–52, 2008.

[80] J. Zhao and A.G. Kosovichev. Helioseismic observation of the structure and dynamics of a rotating sunspot beneath the solar surface. *The Astrophysical Journal*, 591:446, 2003.